AGU ADVANCING EARTH AND SPACE SCIENCES

JGR Earth Surface

RESEARCH ARTICLE
10.1029/2026JF009216

Special Collection:
Aeolian-Fluvial Interactions across the Solar System

Surface Mineralogy and Hydrological Controls on "Hotspots" of Dust Emission at Etosha Pan, Namibia

N. S. Wallum[1], R. G. Bryant[2], G. F. S. Wiggs[1], R. L. Reynolds[3], H. L. Goldstein[3], J. A. Leidelmeijer[3], J. M. Nield[4], and M. C. Baddock[5]

[1]School of Geography and the Environment, Oxford University Centre for the Environment, University of Oxford, Oxford, UK, [2]School of Geography and Planning, University of Sheffield, Sheffield, UK, [3]United States Geological Survey (USGS), Denver, CO, USA, [4]School of Geography and Environmental Science, University of Southampton, Southampton, UK, [5]Department of Geography, Loughborough University, Loughborough, UK

Key Points:

- Dust emissions at Etosha Pan concentrate in hotspots that vary seasonally and inter-annually in response to changes in surface conditions
- The formation and breakdown of evaporite crusts expose fine, erodible sediments that are easily mobilized by wind, contributing to dust emissions
- Seasonal precipitation, flooding, and drying cycles modulate surface moisture and crust stability, which influence dust emission patterns

Supporting Information:

Supporting Information may be found in the online version of this article.

Correspondence to:

N. S. Wallum,
natasha.wallum@ouce.ox.ac.uk

Citation:

Wallum, N. S., Bryant, R. G., Wiggs, G. F. S., Reynolds, R. L., Goldstein, H. L., Leidelmeijer, J. A., et al. (2026). Surface mineralogy and hydrological controls on "hotspots" of dust emission at Etosha Pan, Namibia. *Journal of Geophysical Research: Earth Surface*, *131*, e2026JF009216. https://doi.org/10.1029/2026JF009216

Received 23 MAR 2026
Accepted 16 JUL 2026

Author Contributions:

Conceptualization: N. S. Wallum, R. G. Bryant, G. F. S. Wiggs
Data curation: N. S. Wallum
Formal analysis: N. S. Wallum
Investigation: N. S. Wallum, G. F. S. Wiggs, H. L. Goldstein,

Abstract

Ephemeral lake beds are globally significant sources of atmospheric mineral dust aerosols, yet emissions from these landforms exhibit considerable spatial and temporal variability. The complex interactions between climatic drivers and surface properties that govern dust emissions remain poorly understood, contributing to uncertainties in model predictions of atmospheric dust concentrations and their global effects. In this study, we used multitemporal satellite remote sensing combined with model reanalysis data from 2018 to 2022 to investigate the mineralogical, hydrological, and climatic controls on dust emission "hotspots" at Etosha Pan, Namibia. A record of dust source locations derived from MODIS and MSG-SEVIRI observations was used to identify spatially discrete clusters (hotspots) of recurrent dust emission. Surface mineral composition at these sites was analyzed through linear spectral unmixing of Landsat 8–9 Operational Land Imager data to estimate the relative abundance of evaporite and clay mineral endmembers, with results validated against X-ray diffraction analyses of field-collected sediment samples. Our findings indicate that dust emission hotspots are associated with the formation of evaporite crusts, produced by salt efflorescence following wet-season precipitation and ephemeral flooding. Strong winds during the dry season can disrupt these crusts, exposing large quantities of fine sediments that are extremely susceptible to aeolian entrainment. These results highlight the critical role of surface crust mineralogy, influenced by hydrological history, in controlling dust emission dynamics. This approach provides a transferable framework for identifying and characterizing hydrological and mineralogical controls on dust source regions in other dryland playa environments, with potential applications for improving regional and global dust emission modeling.

Plain Language Summary

When dry, lake beds are significant sources of windblown dust that affect climate, ecosystems, air quality, and human health. However, the amount of dust they release varies depending on weather conditions and their surface properties, making it difficult to predict atmospheric dust levels and their impacts. In this study, we used satellite images and modeled weather data from 2018 to 2022 to understand the causes of dust emissions from Etosha Pan in Namibia, a major dust source in the Southern Hemisphere. We identified where dust originates ("hotspots") and analyzed the minerals present at these sites. Our results show that dust is mainly produced when salt crusts form after flooding during the wet season. In the dry season, strong winds break these crusts apart, releasing fine dust particles into the air. We found that the type of crust and the area's flooding history are key factors controlling dust emissions. This understanding could help improve predictions of dust storms from dry lake beds and potentially help to mitigate their wide-ranging impacts.

1. Introduction

Windblown mineral dust from arid and semi-arid regions is a key component of the Earth's land-atmosphere-ocean-biosphere system, influencing climate, biogeochemistry, and human health (Adebiyi et al., 2023; Middleton & Kang, 2017). Dust alters the global radiation balance (Kok et al., 2023, 2025; L. Li et al., 2025), contributes to ocean fertilization and terrestrial nutrient cycling (Dansie et al., 2022; Hamilton et al., 2022), and degrades air quality and visibility with adverse health effects (Aboagye-Okyere et al., 2025; Prospero et al., 2021; Tong et al., 2023). Given that dust emissions are sensitive to climate and land-use change, a process-based understanding of their surface controls is essential (Hennen et al., 2024; Mona et al., 2023).

Accurately representing dust emissions in atmospheric models remains challenging. Emission processes are nonlinear, reflecting interactions among surface properties, sediment supply, and meteorological forcing (Klose

J. A. Leidelmeijer, J. M. Nield, M. C. Baddock
Methodology: N. S. Wallum, R. G. Bryant
Project administration: N. S. Wallum
Resources: R. G. Bryant, R. L. Reynolds, H. L. Goldstein, J. A. Leidelmeijer
Supervision: R. G. Bryant, G. F. S. Wiggs
Visualization: N. S. Wallum
Writing – original draft: N. S. Wallum
Writing – review & editing: N. S. Wallum, R. G. Bryant, G. F. S. Wiggs, R. L. Reynolds, H. L. Goldstein, J. A. Leidelmeijer, J. M. Nield, M. C. Baddock

et al., 2021). Coarse-resolution inputs and simplified parameterizations lead to systematic errors in the timing, magnitude, and spatial distribution of dust in global and regional models (Kok et al., 2021a, 2021b). These errors underscore the need for field-scale, process-oriented studies to improve model parameterizations of dust source dynamics (Chappell et al., 2023).

Ephemeral lake beds (playas or pans) are globally significant dust sources (Prospero et al., 2002; Song & Ginoux, 2025; Washington et al., 2003; Zucca et al., 2021). These seasonally flooded, internally drained basins accumulate fine-grained sediments through fluvial deposition and evaporative concentration (Shaw & Bryant, 2011). When dry, their salt-enriched, sparsely vegetated surfaces can become highly emissive (Baddock et al., 2021; Goudie, 2018). However, dust models rarely resolve the rapid local-scale processes, including seasonal inundation and desiccation cycles, crust formation and breakdown, and shifting wind erosion thresholds, that strongly influence emissions in these systems (Bucher & Stein, 2016). Limited consideration of these processes in dust emission models persists despite evidence that accounting for such dynamics can substantially improve emission estimates (Banks et al., 2022).

Evaporite crust formation and degradation is a first-order control on playa dust activity. Crust mineralogy and morphology govern both sediment availability and erodibility (Baddock et al., 2011; Gill, 1996; Zhang et al., 2021). Fragile, poorly interlocked sulfate- and carbonate-rich crusts are highly erodible (De Deckker, 2019; Nield, Neuman, et al., 2016; Reynolds et al., 2007, 2009), whereas halite-rich crusts often form harder, cemented surfaces resistant to deflation (Goldstein et al., 2017; Nickling & Ecclestone, 1981). Microstructural properties such as crystal size, shape, and interlocking can be more critical than bulk mineralogy in determining erodibility (Buck et al., 2006, 2011; Lee & Kurtis, 2017). These properties vary dynamically with hydroclimatic conditions (Dai et al., 2022; King et al., 2011; Milewski et al., 2019). Yet most models neglect these interacting controls, leaving emission processes poorly constrained (Karami et al., 2021; Sweeney et al., 2022). As a result, they fail to capture small (1–10 km) and highly localized sub-basin scale dust emission "hotspots" that produce intense, discrete dust plumes that can merge into regional-scale events (Gillette, 1999; Walker et al., 2009).

Etosha Pan in northern Namibia is among the most active dust-emitting playas in the Southern Hemisphere (Formenti et al., 2019; Vickery et al., 2013). Satellite observations have shown that dust emissions from Etosha Pan are highly seasonal and spatially discrete, driven by rainfall variability, flooding, surface drying, and wind conditions (Wallum et al., 2025). Field studies have confirmed the presence of evaporite-rich sediments and salt crusts at Etosha Pan (e.g., Bhattachan et al., 2015; Buch & Rose, 1996; Z. Li et al., 2018), and recent work has examined dust emission processes at the source (Clements & Washington, 2021; Wallum et al., 2026; Wiggs et al., 2022). However, the specific linkages between surface mineralogy, hydrology, and dust emission remain poorly resolved at sub-basin scale.

In this study, we address this gap by analyzing the mineralogical, hydrological, and climatic controls on discrete dust emission hotspots at Etosha Pan from 2018 to 2022. We combine multitemporal satellite remote sensing, X-ray diffraction (XRD) of surface sediments, and climate reanalysis data to: (a) identify the locations and surface characteristics of dust emission hotspots relative to non-emissive areas; (b) quantify the mineral composition of hotspot surfaces using linear spectral unmixing (LSU) validated against XRD data; and (c) assess the hydrological and climatic drivers of hotspot formation, capturing spatial and temporal variability in surface conditions and emission activity. Our results provide new insights into the processes controlling dust emissions from ephemeral lake beds and support improved representation of these dynamic sources in both Earth system and regional dust models.

2. Study Area

Etosha Pan is a ~4,800 km^2 endorheic basin situated in northern Namibia (Figure 1). It forms the terminal depositional environment of the Cuvelai-Etosha drainage system, which spans ~130,000 km^2 across southern Angola and northern Namibia (Mendelsohn et al., 2013; Miller, 1997). Seasonal rainfall during the austral summer (November to March) generates a network of ephemeral channels, locally known as *iishana* (plural) or *oshana* (singular), that converge into the Ekuma River and discharge into the northwestern margin of the pan. Additional inflows may occasionally originate from the Oshigambo, Oshangulu, and Owambo Rivers, contributing runoff to the northern and eastern sectors of the basin (Hamunyela et al., 2022; Hipondoka et al., 2018). These ephemeral systems are considered the primary source of fine-grained fluvial sediments delivered to the pan during periods of shallow inundation (Bryant, 2003; Mahowald et al., 2003).

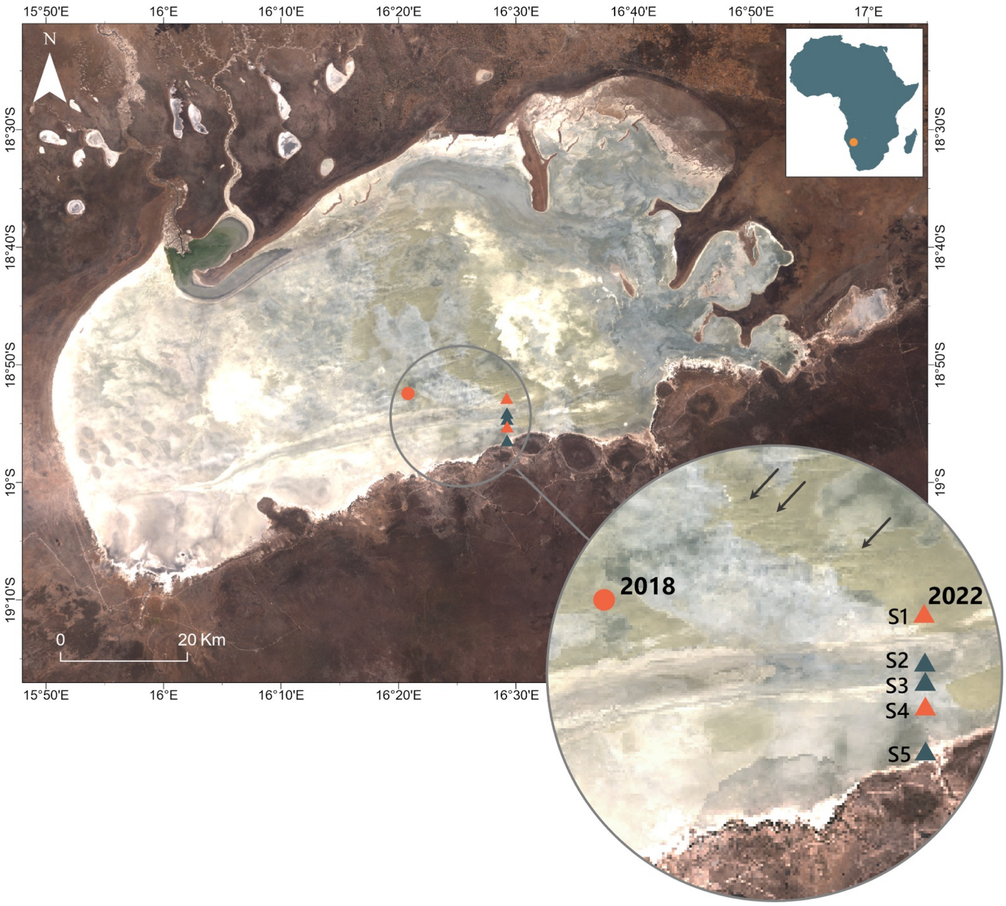

Figure 1. Location of Etosha Pan, Namibia. The inset shows sediment sampling sites at dust emission hotspots (orange) and non-emissive areas (blue), sampled in 2018 and 2022 (Sites 1–5; see Table S1 in Supporting Information S1 for descriptions). The background is a true-color Landsat 8 Operational Land Imager image acquired on 5 July 2018, showing westward-moving dust plumes emanating from hotspot sources (indicated by arrows).

During the dry austral winter (March to October), the water table declines and surface water evaporates, exposing extensive areas of the pan floor. The exposed surface comprises predominantly fine-grained, clay- and silt-rich sediments of the Andoni Formation (Miller et al., 2010; Pickford et al., 2009) interspersed with widespread evaporite (salt) deposits formed under arid conditions (Bhattachan et al., 2015; Buch & Rose, 1996; Hipondoka et al., 2014; Rahm & Buch, 1997). These surface materials exhibit pronounced spatial heterogeneity and seasonal variability in mineralogical composition, moisture content, and crust development. Due to extreme salinity and limited water availability, vegetation is sparse (Cunningham & Jankowitz, 2010), and exposed sediments are highly susceptible to aeolian erosion under the prevailing E-NE winds, frequently leading to the development of intense dust emission events (Murray et al., 2016; Vickery et al., 2013; Wallum et al., 2025; Wiggs et al., 2022).

3. Data and Methods

3.1. Dust Source Hotspot Mapping and Surface Classification

A 20-year record (2000–2022) of dust source point locations over Etosha Pan, derived from MODIS Collection 6.1 (MOD09GA/MYD09GA) and MSG-SEVIRI imagery (Wallum, 2025a), was used to identify statistically significant clusters of points that delineated dust source areas (hotspots) at the sub-basin scale through Average Nearest Neighbor (ANN) analysis (Kandakji et al., 2020) in ArcGIS Pro® 3.4 (Esri®, Redlands, CA). These hotspot regions were subsequently examined using Landsat imagery to characterize surface conditions and their temporal evolution. Moderate-resolution Landsat 8–9 Operational Land Imager (OLI) satellite imagery (30 m spatial, 8-day temporal resolution) was then used to characterize the surface properties of these dust hotspot clusters and to compare them with non-emissive regions during the 2018–2022 period. Since Landsat acquisitions occurred at discrete intervals, image dates were not required to coincide exactly with individual MODIS/MSG-SEVIRI dust plume observations. Rather, the Landsat time series was used to examine changes in surface conditions within hotspot regions associated with recurrent dust emission activity. A total of 74 cloud-free Landsat 8–9 OLI Collection 2 Level-2 surface reflectance scenes covering the austral winter dry (dust) seasons (March–October) from 2018 to 2022 were obtained from the U.S. Geological Survey Earth Explorer data portal (www.earthexplorer.com). Each scene comprised nine spectral bands in the VNIR–SWIR range (0.4–2.5 μm). A complete list of image acquisition dates and scene identifiers is provided in Table S2 in Supporting Information S1.

False-color composite (bands 5, 4, 3) image time series were generated to enhance visual discrimination of sediment surface conditions based on spectral response. These composites were examined throughout the 2018–2022 study period to identify temporal and spatial variations in surface texture, color, and morphology associated with the development of recurrent dust emission hotspots.

3.2. Geochemical Analysis and Mineral Mapping by Spectral Unmixing

To quantify surface mineral composition, a fully constrained LSU model was applied to the Landsat 8–9 OLI image series from 2018 to 2022. This supervised approach estimates sub-pixel abundances of distinct mineral phases by modeling each pixel's reflectance as a linear, additive combination of predefined "pure" spectra (endmembers) weighted by their fractional contributions (Ferrier et al., 2002; Kodikara et al., 2023; Settle & Drake, 1993). Fully constrained LSU ensures physically meaningful results by enforcing non-negativity and abundance sum-to-unity constraints (Bryant, 1996; Jin et al., 2019). The approach is well suited to ephemeral playa environments, where mineral assemblages form through predictable hydrochemical precipitation pathways, as determined by groundwater chemistry and evaporation sequences (Drake et al., 1994; Hubbard & Crowley, 2005; Milewski et al., 2020).

Unlike unsupervised or machine learning classifiers, LSU allows direct quantification of specific minerals, has lower computational overhead, handles noise and residual spectral variation effectively, and supports iterative time-series analysis, making it especially well-suited for monitoring mineralogical changes linked to hydrological and climatic variability (Milewski et al., 2017). While hyperspectral sensors (e.g., Hyperion, EMIT, PRISMA) offer higher spectral resolution and enhanced mineral discrimination (Cogliati et al., 2021; Green et al., 2019, 2023; Kodikara et al., 2012), their spatial and temporal coverage over Etosha are currently limited. In contrast, the consistent revisit frequency and moderate spatial resolution (30 m) of Landsat 8–9 OLI multispectral data provided a practical balance of spectral detail and temporal coverage for resolving mineralogical change across the 2018–2022 study period (Kruse & Perry, 2013; Radwin & Bowen, 2021).

LSU model calibration and validation were based on XRD analyses of 20 surface sediment samples collected during field campaigns in July–September 2018 and September 2022, respectively (Figure 1 and Table S1 in Supporting Information S1). Samples represented three sediment types: surface crust (0–2 cm), subsurface sediment (2–5 cm), and ripple features (0–0.1 cm). The 2018 campaign focused on a single emissive hotspot in the central pan region during peak and late dust season phases to assess intra-seasonal compositional variability associated with dust activity. In 2022, five sites were strategically sampled along a transect sampling variable hydrological conditions (from frequently inundated to dry salt-encrusted surfaces) and surface emissivities (ranging from non-emissive to highly emissive hotspot regions) along the southern pan margin (Table S1 in Supporting Information S1). Site selection was informed by prior remote sensing analysis to capture representative variability of surface conditions and presumed sediment mixtures on the pan while ensuring field accessibility.

XRD analysis of air-dried, <2 mm sieved sediment samples was conducted using an X'Pert PRO diffractometer (PANalytical BV, Almelo, the Netherlands). Diffractograms were processed using HighScore software (PANalytical BV), enabling both qualitative phase identification and semi-quantitative determination of mineralogical composition (by weight %) for each sample. The mineral content identified through XRD analysis of surface sediments collected during field campaigns in July and September 2018 formed the basis for selecting spectral endmembers used in the LSU model. Eight dominant mineral phases were identified based on their consistent occurrence across samples and distinct spectral features: halite (NaCl), calcite ($CaCO_3$), gypsum ($CaSO_4 \cdot 2H_2O$), thenardite (Na_2SO_4), muscovite [$KAl_2(AlSi_3O_{10})(F,OH)_2$], analcime ($NaAlSi_2O_6 \cdot H_2O$), montmorillonite [(Na,

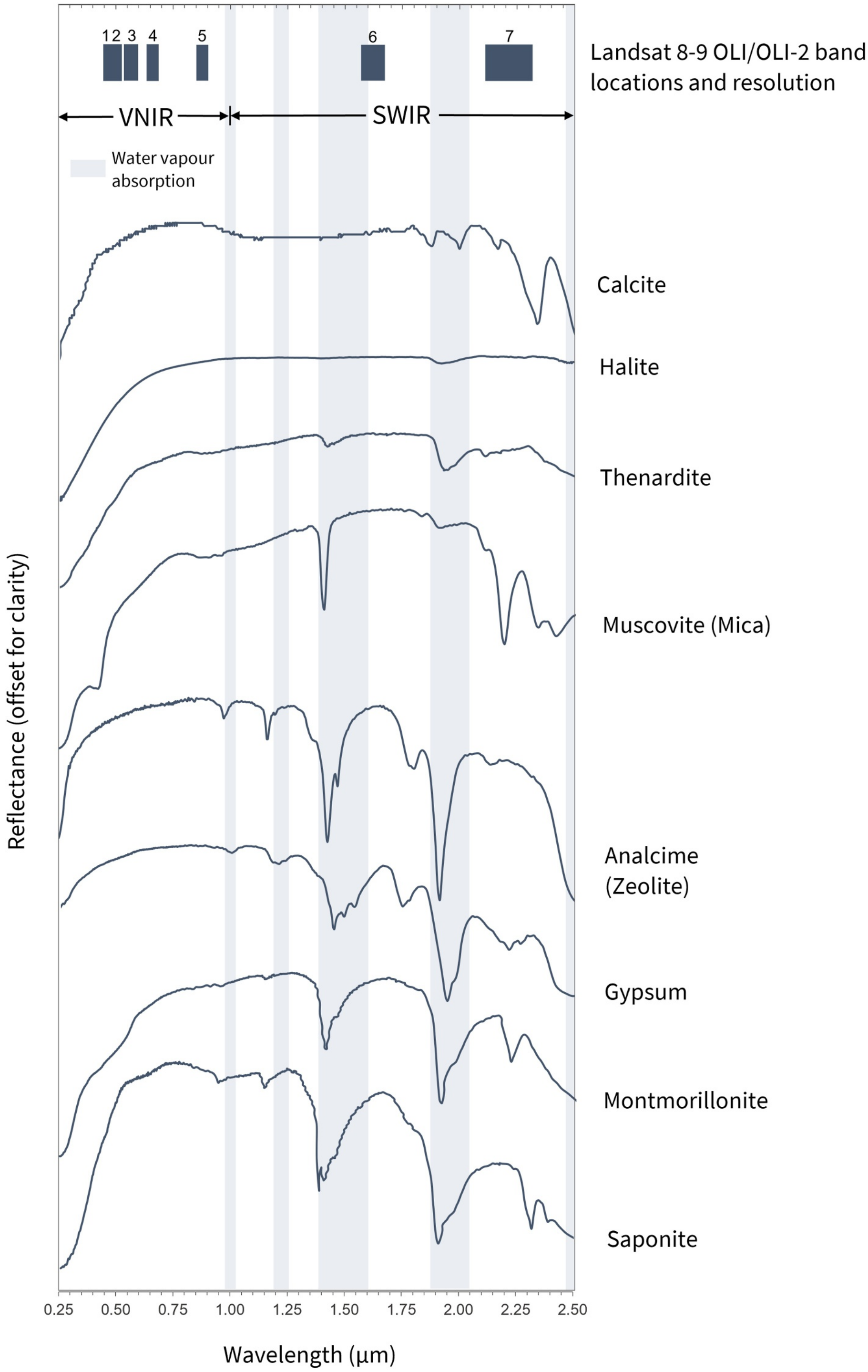

Figure 2. VNIR–SWIR reflectance spectra for the eight mineral endmembers identified from X-ray diffraction analyses of surface sediments at Etosha Pan and used in the linear spectral unmixing model. Markers indicate the spectral positions and bandwidths of the Landsat 8–9 Operational Land Imager bands used in the analysis.

Ca)$_{0\cdot33}$(Al,Mg)$_2$Si$_4$O$_{10}$·nH$_2$O], and saponite [(½Ca,Na)$_{0\cdot33}$(Mg,Fe^{2+})$_3$(Si,Al)$_4$O$_{10}$(OH)$_2$·4H$_2$O]. Spectral signatures for each endmember were sourced from the USGS Spectral Library (Kokaly et al., 2017). The VNIR–SWIR reflectance spectra of the selected mineral endmembers are shown in Figure 2 together with the spectral positions of the Landsat 8–9 OLI bands used in the unmixing analysis. The endmembers were grouped into (a) evaporite

Table 1
Mineral Endmembers Used in Linear Spectral Unmixing, Grouped by Mineral Type

Group	Mineral	Chemical formula	Mineral type
(i) Evaporite minerals	Halite	NaCl	Sodium chloride (evaporite)
	Calcite	$CaCO_3$	Calcium carbonate (carbonate evaporite)
	Gypsum	$CaSO_4{\cdot}2H_2O$	Calcium sulfate dihydrate (sulfate evaporite)
	Thenardite	Na_2SO_4	Sodium sulfate (anhydrous evaporite)
(ii) Clays and related silicates	Muscovite	$KAl_2(AlSi_3O_{10})$ $(F,OH)_2$	Potassium mica (phyllosilicate)
	Analcime	$NaAlSi_2O_6{\cdot}H_2O$	Sodium aluminosilicate (zeolite)
	Montmorillonite	$(Na,Ca)_{0{\cdot}33}(Al,Mg)_2Si_4O_{10}{\cdot}nH_2O$	Smectite-group clay (aluminosilicate)
	Saponite	$(½Ca,Na)_{0{\cdot}33}(Mg,Fe^{2+})_3(Si,Al)_4O_{10}(OH)_2{\cdot}4H_2O$	Smectite-group clay (magnesium-rich aluminosilicate)

minerals and (b) clays and related silicates (Table 1). This classification reflects both geochemical origin and stratigraphic distribution. Evaporite minerals (e.g., halite, calcite, thenardite), formed by evaporation of surface and shallow (0–3 m) groundwater, were concentrated in surface crusts (Table S3). Clay and silicate minerals (e.g., montmorillonite, analcime, saponite) were more prevalent in subsurface and ripple samples (Table S3), likely due to accumulation of fine detrital material and early diagenetic alteration through porewater interactions (Shaw & Bryant, 2011). This vertical mineral layering, characteristic of ephemeral saline lakebeds, significantly influences both the spectral reflectance properties and erodibility of surface materials (Drake et al., 1994; Goldstein et al., 2017; González-Romero et al., 2024).

Linear spectral unmixing was then applied to Landsat 8–9 OLI surface reflectance data from the 2018–2022 austral winter dry seasons (Figure 3). Image pre-processing involved masking vegetation and surface water using the Normalized Difference Vegetation Index (NDVI; Rouse et al., 1973) and Modified Normalized Difference Water Index (MNDWI; Xu, 2006). The constrained LSU model, implemented in ENVI® 6.1 (Harris Geospatial®, Boulder, CO), performed least squares fitting of the endmember spectra to reflectance values in bands 1–7 of the unmasked Landsat pixels, with mineral abundances constrained to sum to 100%. The model generated one abundance map per mineral endmember per scene in the Landsat 8–9 OLI image time series, with output values representing the estimated percent surface composition (0%–100%) of each mineral endmember within each pixel. Mineral abundance maps were rendered as RGB (red-green-blue) composites to visualize the spatiotemporal trends of key mineral phases across dust seasons (Figure 3).

Model validation was performed by comparing LSU-predicted mineral abundances with XRD-derived compositions from an independent set of sediment samples collected in September 2022. These samples were not used in the definition or calibration of the spectral endmembers, which were derived exclusively from 2018 XRD data, thereby ensuring an unbiased, out-of-sample validation with no information leakage between training and evaluation data sets. Statistically significant correlations across all mineral phases ($R^2 = 0.76$, $p < 0.001$) confirmed the robustness and predictive accuracy of the unmixing model (Bryant, 1996; White & Eckardt, 2006; Jin et al., 2019; Milewski et al., 2019; see Text S1 in Supporting Information S1).

3.3. Hydrological and Meteorological Drivers of Emissivity

To assess the hydrological and climatological influences on pan surface properties and dust emissivity, the Landsat 8–9 OLI imagery and mineralogical maps were compared with surface wetness indicators and climate data across the 2018–2022 dust seasons.

Daily time series of surface inundation extent and frequency derived from MODIS satellite data (Wallum, 2025a) were used to characterize hydrological conditions for emission hotspots and non-emissive regions. Daily precipitation inputs were obtained from the Integrated Multi-Satellite Retrievals for GPM (GPM-IMERG) gridded precipitation data set, with a spatial resolution of $0.1° \times 0.1°$, accessed via NASA's Goddard Earth Sciences Data and Information Services Center (http://disc.gsfc.nasa.gov/).

Atmospheric conditions were evaluated using ERA5-Land reanalysis data produced by the European Centre for Medium-Range Weather Forecasts (ECMWF) (Muñoz Sabater, 2019; Muñoz-Sabater et al., 2021). Hourly estimates of 2 m air temperature, 2 m dew point temperature, and 10 m horizontal (u) and vertical (v) wind

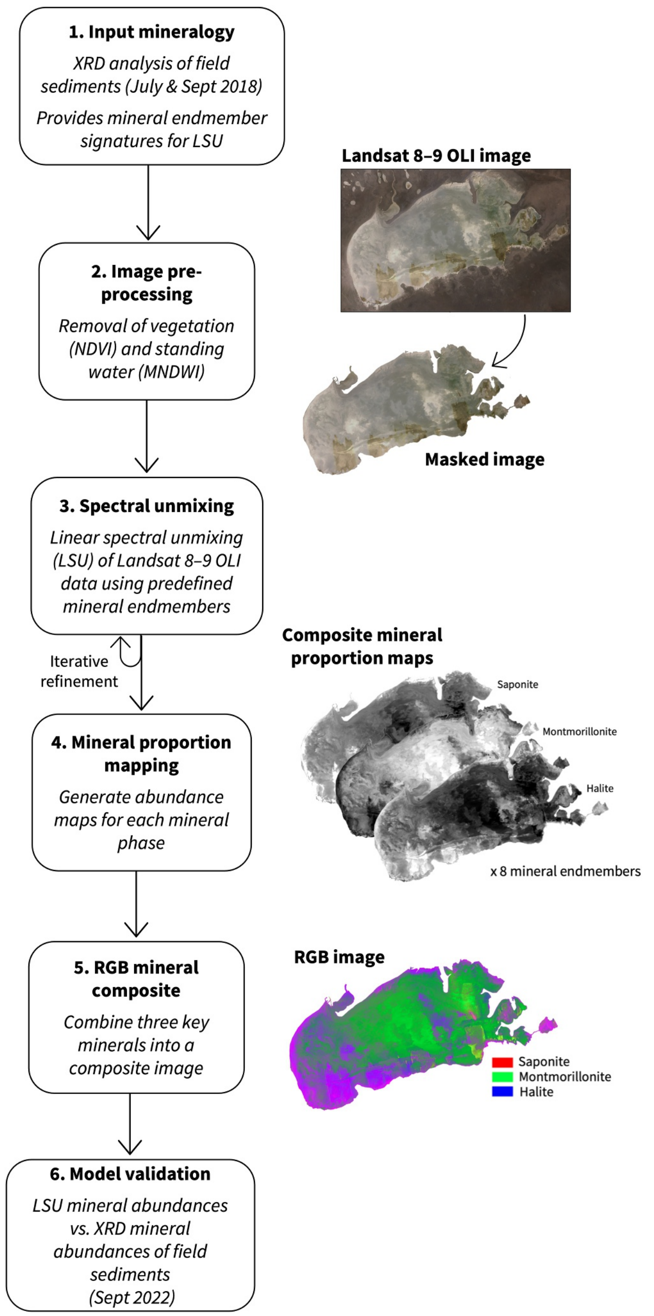

Figure 3. Workflow diagram illustrating the processing pathway for mineral mapping using a fully constrained linear spectral unmixing method on Landsat 8–9 Operational Land Imager data.

components were extracted for Etosha Pan from the Copernicus Climate Change Service Data Store (https://cds.climate.copernicus.eu/). Relative humidity (RH, in %) was calculated from 2 m air temperature (t) and 2 m dew point temperature (t_d) using the revised Magnus (1844) formula:

$$\mathrm{RH} = 100 \times \left(\frac{e^{\frac{\beta \times t_d}{\lambda + t_d}}}{e^{\frac{\beta \times t}{\lambda + t}}} \right) \tag{1}$$

where $\beta = 17.625$ and $\lambda = 243.04$°C (Alduchov & Eskridge, 1996; Lawrence, 2005; Mateus et al., 2021). Calculated u and v vector components were corrected with relevant off-set and scaling factors, from which wind speed ($ws = \sqrt{u^2 + v^2}$, in m s^{-1}) was calculated. Hourly values were aggregated to produce daily mean time series to enable direct comparison with the daily dust emission and hydrological data sets used in this study.

The resulting daily time series of hydroclimatic parameters were analyzed alongside satellite-derived surface changes (i.e., variations in color, texture, and mineral composition) to identify environmental drivers associated with the formation and persistence of dust-emissive surface conditions on the pan.

4. Results and Discussion

4.1. Identification of Dust Emission Hotspots

Statistical point pattern analysis of dust plume source locations between 2018 and 2022 revealed significant spatial clustering of emissions at the sub-basin scale (Figure 4). These clusters consistently originated from a limited number of discrete regions toward the central part of Etosha Pan. Such localized, high-frequency emission zones (hotspots) emerged as visually distinctive features on the pan surface in Landsat 8–9 OLI false-color composites (bands 5, 4, 3), particularly during the relatively dry and highly emissive years of 2018, 2019 and 2022 (Figure 4a). Hotspot regions appeared as brown-toned surface patches with distinct color and texture contrasts relative to surrounding areas, indicative of altered surface conditions. In contrast, these features were absent during the relatively wetter, non-emissive years of 2020 and 2021 (Figure 4b), underscoring their temporal variability and association with active dust emission years (see Section 4.3).

Of the 91 dust emission days recorded during the 2018–2022 analysis period, the majority (83 dust days) were directly linked with dust plumes recorded by MODIS and MSG-SEVIRI during the 2018–2022 analysis period originating from ANN-defined localized hotspot regions. On days with active dust emission that coincided with Landsat 8–9 OLI acquisitions, dust plumes were consistently observed emanating from these distinct surface patches, further evidencing their role as dominant dust source regions. However, the size and distribution of these hotspot regions varied between emissive years. In 2019, hotspots expanded to diameters of up to 30 km, forming more extensive and dispersed emission zones compared to the smaller, more clustered hotspots observed in 2018 and 2022, which typically ranged from 1 to 10 km in diameter (Figure 4a).

Despite interannual variability in areal extent, a consistent trend observed across all emissive years was the enlargement of hotspot areas following major dust emission events. This pattern suggests a positive feedback whereby the expansion of hotspot regions increases the area of exposed, erodible sediments available for wind erosion, promoting the emission of additional dust plumes and further hotspot growth (see Section 4.2 for discussion of the associated surface mineralogical changes). Consequently, years characterized by more extensive

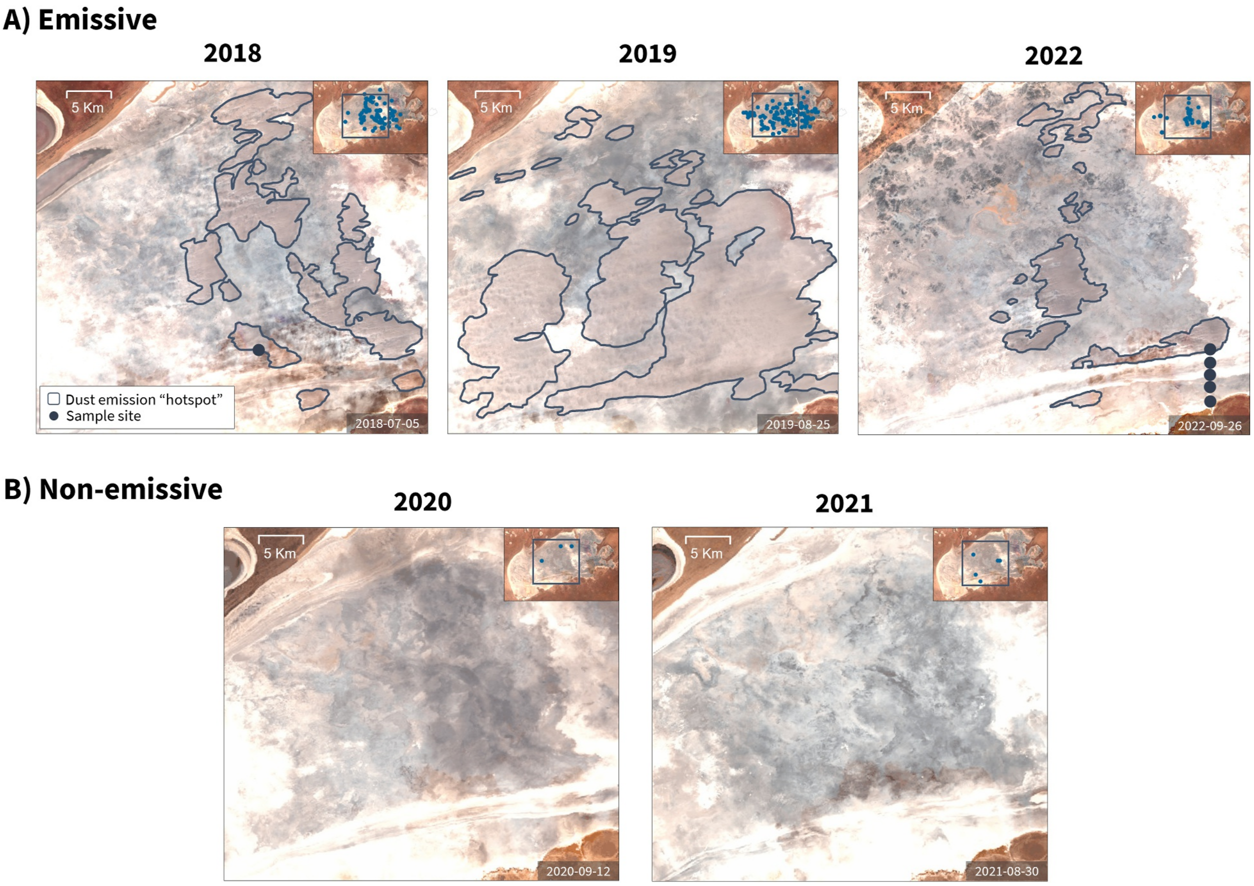

Figure 4. Landsat 8–9 Operational Land Imager false-color (bands 5, 4, 3) image composites of Etosha Pan showing (a) the occurrence and distribution of dust plumes sourced from emission hotspots (polygons) during emissive years (2018, 2019 and 2022) and (b) non-emissive years (2020 and 2021). Locations of field sample sites are indicated on the 2018 and 2022 imagery and in Figure 1 and Table S1 in Supporting Information S1. Insets show all dust plume source points identified from MODIS and MSG-SEVIRI observations during the corresponding dry season (March–October) of each year (Wallum et al., 2025).

hotspot development corresponded with increased dust emission activity. In 2019 (the most emissive year), 107 dust plume events were recorded across 54 dust days, coinciding with the largest combined hotspot extent on the pan surface (1,261 km^2; ~26% of the total pan area). In comparison, fewer plume events were recorded from smaller and more clustered hotspot regions in 2018 (42 plume events over 25 dust days; maximum hotspot area: 491 km^2, ~10% of the total pan area) and 2022 (22 events over 10 dust days; maximum hotspot area: 95 km^2, ~2% of the total pan area). These results demonstrate a strong relationship between the spatial dynamics of hotspot regions and the magnitude and frequency of dust emissions from Etosha Pan.

4.2. Surface Mineralogy of Dust Emission Hotspots

Comparative RGB composite map time series highlight pronounced differences in the distribution of dominant mineral phases (saponite, montmorillonite, and halite) across the pan surface during the relatively dry, emissive 2018 dry season and the wetter, non-emissive 2021 dry season (Figures 5 and 6; see Figures S3–S5 in Supporting Information S1 for 2019, 2020, and 2022 time series).

The temporal evolution of emissive hotspot regions in Landsat 8–9 OLI false-color composites is illustrated in Figure 5 alongside corresponding RGB mineral abundance maps generated from LSU. Time slices were selected from the Landsat image time series to provide representative coverage of early-, mid-, and late-season surface conditions and key stages of hotspot development throughout the dust season (see Figure S2 in Supporting Information S1 for seasonal image sequences from all study years). The RGB composites for the 2018 dust season suggest that bright blue tones in early-season composites (Figure 5a) reflect the formation of an extensive halite (evaporite) crust following the austral summer wet season. As the austral winter dry season progressed

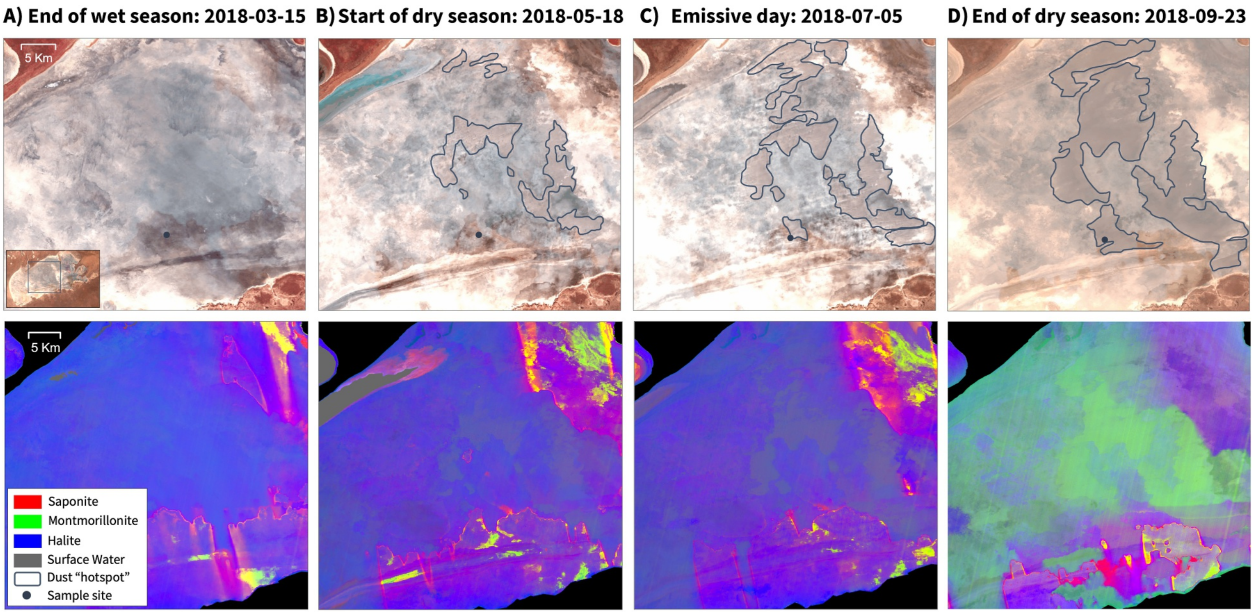

Figure 5. Temporal comparisons of Landsat 8 Operational Land Imager (OLI) false-color composite (bands 5, 4, 3) images of surface change at Etosha Pan across the 2018 winter dry season showing the development of dust emission hotspots (outlined in upper panels), and linear spectral unmixing model output RGB image composite maps (lower panels) for corresponding image dates, where RGB channels delineate estimates of relative mineral abundances (%) for saponite (Red), montmorillonite (Green) and halite (Blue) minerals, respectively. Note: Some linear or vivid bright features in the northeast and southern portions of the unmixing outputs are sensor-related artifacts associated with Landsat OLI image processing.

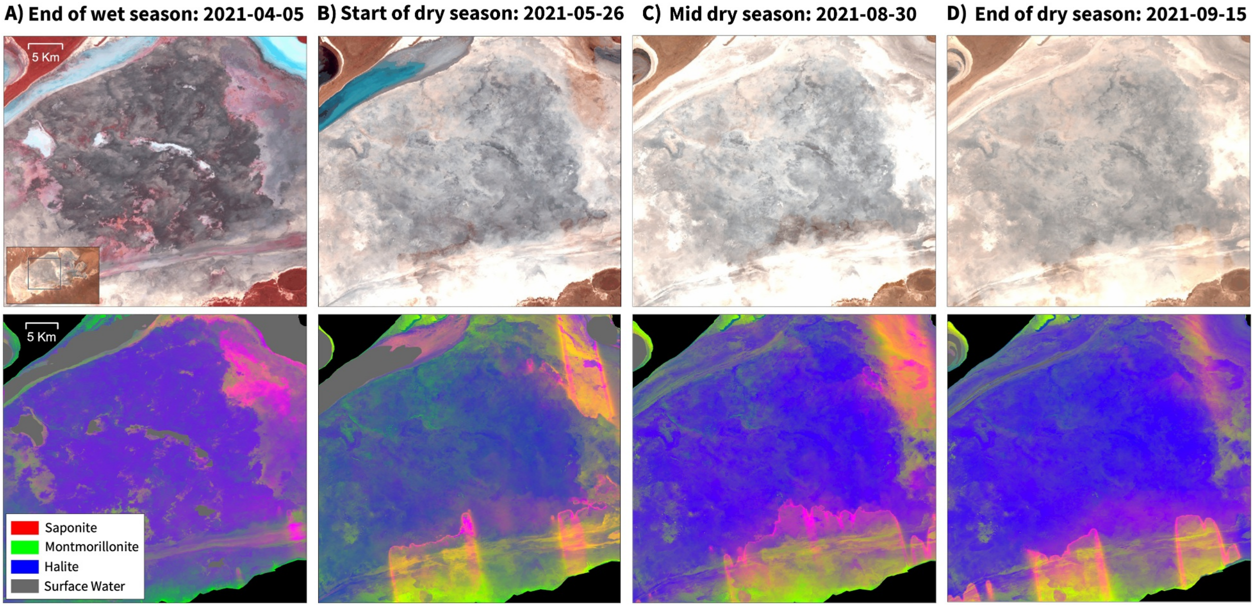

Figure 6. Temporal comparisons of Landsat 8 Operational Land Imager (OLI) false-color composite (bands 5, 4, 3) images of surface change at Etosha Pan across the 2021 winter dry season (upper panels) and linear spectral unmixing model output RGB image composite maps (lower panels) for corresponding image dates, where RGB channels delineate estimates of relative mineral abundances (%) for (R) saponite, (G) montmorillonite and (B) halite minerals, respectively. Note: Some linear or vivid bright features in the northeast and southern portions of the unmixing outputs are sensor-related artifacts associated with Landsat OLI image processing.

Table 2
X-Ray Diffraction (XRD) Results for Surface Crust and Sediment Samples Acquired From Dust Emission Hotspots in July and September 2018 and Dust Emission Hotspots (Sites 1 and 4) in September 2022, Showing Abundances for Dominant Mineral Types (Endmembers) Used in Spectral Unmixing Analysis

	Sample ID										
							September 2022				
	July 2018			September 2018			(Site 1)			(Site 4)	
	CS	SS	RS	CS	SS	RS	CS	SS	RS	CS	SS
Mineral	% (v/v)										
Analcime (zeolite) ($NaAlSi_2O_6 \cdot H_2O$)	28.4	45.6	46.5	29.0	45.0	11.0	32.0	7.0	25.0	24.0	34.0
Calcite ($CaCO_3$)	17.8	30.8	34.9	12.0	6.0	13.0	12.0	9.0	14.0	11.0	15.0
Gypsum ($CaSO_4 \cdot 2H_2O$)	1.0	2.2	–	–	–	–	–	–	–	–	–
Halite (NaCl)	43.9	8.7	6.1	–	–	3.0	27.0	26.0	10.0	–	–
Montmorillonite [$(Na,Ca)_{0.33}(Al,Mg)_2Si_4O_{10} \cdot n(H_2O)$]	7.8	11.0	10.7	–	–	–	–	4.0	–	–	–
Muscovite [$(KAl_2(AlSi_3O_{10})$ $(F,OH)_2$]	–	–	–	39.0	25.0	45.0	–	29.0	32.0	20.0	28.0
Saponite [$(½Ca,Na)_{0.33}(Mg,Fe^{2+})_3(Si,Al)_4O_{10}(OH)_2 \cdot 4H_2O)$]	1.1	1.7	1.8	Trace	–	–	–	6.0	–	–	–
Thenardite (Na_2SO_4)	Trace	Trace	Trace	–	–	–	–	–	–	–	–

Note. For the location of field sample sites, see Figure 1. XRD results for all mineral types present in (emissive and non-emissive) field sediment sample sites are given in Table S3. CS = Crusted surface (0–2 cm depth); SS = Soft subsurface (2–5 cm depth); RS = Rippled surface features.

(Figures 5b–5d), increasing green tones in identified hotspot areas indicated enhanced surface exposure of montmorillonite-rich sediments, particularly following major dust emission events. Concurrently, the halite signal diminished in these regions while remaining dominant in surrounding non-emissive areas. Similar trends were observed in emissive years 2019 and 2022 (Figures S3 and S5 in Supporting Information S1), suggesting that the absence or degradation of evaporite surface crusts, coupled with increased clay mineral exposure, is characteristic of highly emissive zones on the pan surface. This seasonal shift in mineralogical composition is consistent with the progressive exposure of clay- and silicate-rich subsurface and surface wind ripple sediments following degradation of the overlying evaporite crust, rather than widespread accumulation of newly deposited material at the surface, as documented by field observations at Etosha Pan (Wallum et al., 2026).

Observed differences in surface mineralogy correspond with the distinct color and texture of emissive hotspot areas relative to their surroundings, as detected in the false-color satellite imagery. The prominence of green tones in these regions in the RGB composites reflects higher surface concentrations of montmorillonite, consistent with exposure of underlying clay- and silicate-rich sediments. This interpretation is supported by XRD analysis of crust and near-surface samples collected from hotspot regions at the end (September) of the 2018 and 2022 dry seasons, which identified analcime (zeolite), muscovite, and montmorillonite as dominant mineral phases (Table 2).

Although saponite and montmorillonite were not consistently dominant in XRD analyses, they frequently appeared as major components in the spectral unmixing outputs. This apparent overrepresentation reflects the limited number of predefined endmembers, which grouped spectrally similar minerals into the closest matching category (e.g., montmorillonite or saponite), even though they represent a broader suite of spectrally similar minerals in the sediments, including smectites (e.g., nontronite) and other silicate phases (e.g., loughlinite, phlogopite, orthoclase; Table S3). These minerals exhibit overlapping absorption features near 1.4, 1.9, and 2.2 μm in the VNIR–SWIR range, constraining their discrimination as discrete phases independent of endmember selection (Figure 2; Kokaly et al., 2017). SEM–EDX analysis (Breit, 2022) further shows that montmorillonite and saponite commonly form thin coatings on analcime grains, obscuring diagnostic absorption features. Since LSU assumes pixel reflectance is a linear combination of surface-dominated endmember spectra (Ferrier et al., 2002; Settle & Drake, 1993), such coatings can lead to misclassification of analcime-rich sediments as smectite clays. These factors contribute to systematic misclassification bias in LSU-derived maps (Bryant, 1996; Crowley, 1991; Milewski et al., 2020). Even with more comprehensive endmembers or unsupervised approaches, the moderate spectral resolution of Landsat 8–9 OLI limits phase-level discrimination (Kruse & Perry, 2013).

Consequently, LSU outputs are best interpreted as indicators of broader clay- and silicate-rich surface composition rather than precise mineral abundances at specific points.

In contrast, the RGB composites for the non-emissive 2021 dry season exhibit markedly different surface mineral dynamics (Figure 6). Surface moisture was still evident toward the end of the wet season in April, with grey tones indicating residual surface water in isolated regions (Figure 6a). As the dry season progressed, bright blue tones became more widespread across the pan surface, indicating the later development of a halite-rich crust that persisted through August and September (Figures 6b–6d). A similar pattern of delayed halite crust formation was observed during the non-emissive 2020 dry season (see Figure S4 in Supporting Information S1).

The RGB composite maps and XRD data together confirm halite as the predominant evaporite mineral phase on the pan surface in both emissive and non-emissive years (Figures 5 and 6), with measured abundances in crust and surface sediments ranging from 3.0% to 43.9% (Table 2). Calcite was also consistently detected, with abundances of 6%–35% across crusted and subsurface samples. Halite predominance in spectral unmixing outputs reflects its efflorescence at the uppermost surface layers driven by evaporative concentration of shallow brines, resulting in a stronger spectral expression relative to other evaporite minerals. By contrast, calcite exhibits a more vertically distributed contribution, present across both crusted and subsurface sediments (Table 2). These findings are consistent with previous investigations at Etosha Pan that reported halite and other evaporite minerals in surface crusts and groundwater. Buch and Rose (1996) identified and analyzed thin surface crusts along the pan margins, recovering stable evaporite phases including halite (NaCl), thenardite (Na2SO4), trona (Na3(CO3) (HCO3)·2H2O), and hanksite (Na22K(SO4)9(CO3)2Cl) through brine crystallization. Rahm and Buch (1997) also found strong geochemical signatures for sodium (Na), potassium (K), chloride (Cl-), sulfate (SO_4) and bicarbonate (HCO_3) in sediment samples. More recently, Bhattachan et al. (2015) analyzed a salt sample from the surface of Etosha Pan and found a clear Cl/SO_4 component, which they attributed to halite, thenardite, or double salts such as sulphohalite. Z. Li et al. (2018) investigated the geochemistry of regional groundwater, noting the likely occurrence of halite and sodium phases in the brine underlying the pan. However, these prior studies primarily focused on borehole or pan-margin samples, whereas the current study is the first to report mineralogical data directly from known dust emission sources in the central pan region.

The implications of mineralogical composition for dust emissivity have been widely recognized in the literature (e.g., Buck et al., 2011; Langston & McKenna Neuman, 2005; Nickling & Ecclestone, 1981; Nield, Neuman, et al., 2016; Nield, Wiggs, et al., 2016). Efflorescent mixed halite crusts are common in several major playa dust sources globally (Bowen et al., 2017; R. Li et al., 2020; Mees & Singer, 2006; Milewski et al., 2017, 2019, 2020) and while sulfate and other carbonate salts such as thenardite and trona often form soft, porous "puffy" or "hairy" crusts that are highly susceptible to wind erosion (Buck et al., 2011; Goodall et al., 2000; Teller & Last, 1990), halite-calcite crusts can reduce emission potential by cementing sediment particles and increasing threshold friction velocity (Crowley, 1991; Sweeney et al., 2011). However, crusts that form directly after brief inundation or wetting during the early dry season are often friable and prone to cracking upon drying, producing aggregates small enough to be saltated and potentially destabilizing the surface further (Gillette et al., 2001; Reynolds et al., 2007, 2009; Sweeney et al., 2011). This mechanism may explain why dust emissions in Etosha Pan frequently originate from areas where a halite-calcite crust forms following ephemeral wetting early in the dry season (i.e., March to April) but later breaks down, exposing subsurface sediments rich in silicate minerals (Figure 5; see also Figures S3 and S5 in Supporting Information S1). By contrast, in non-emissive years such as 2020 and 2021, halite crust development appears delayed until later in the dry season (i.e., June to September), potentially forming a denser, more coherent crust resistant to wind erosion (Figure 6; see also Figure S4 in Supporting Information S1).

4.3. Hydrological and Meteorological Drivers of Emissivity

Satellite remote sensing analyses of surface morphology and mineralogy across Etosha Pan indicate that dust emission hotspots are closely linked to changes in surface mineralogy, particularly the disruption of evaporite crusts. The formation and subsequent breakdown of these evaporative mineral crusts is widely recognized as a primary control on dust emissions from ephemeral desert playas globally (e.g., Baddock et al., 2009, 2011, 2015; Bullard et al., 2008; Klose et al., 2019; Macpherson et al., 2008; Nield et al., 2015, 2016a; Niemeyer et al., 1999; Reynolds et al., 2007, 2009; Sweeney et al., 2011, 2016). Characterizing the environmental controls on the

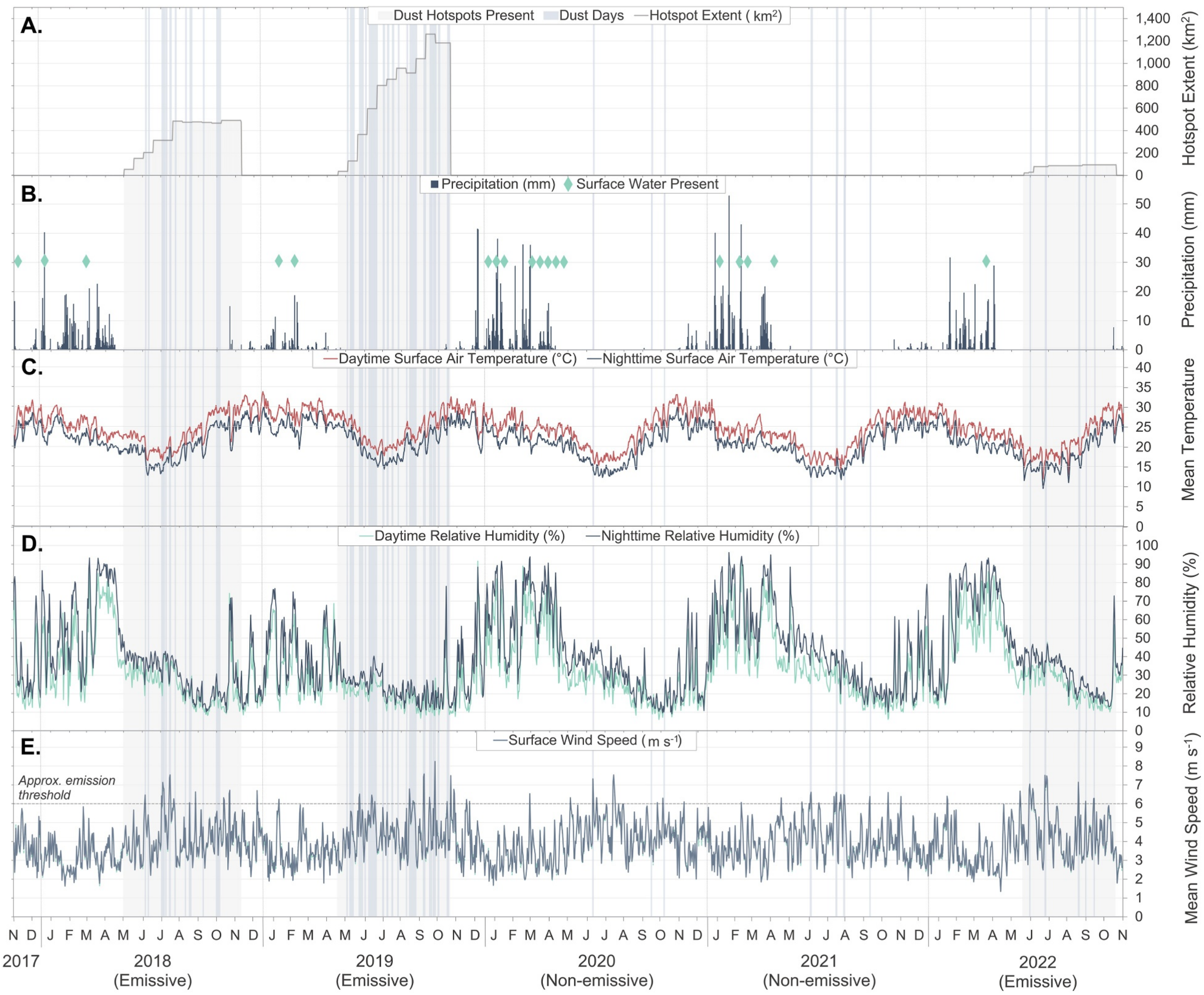

Figure 7. Daily time series of (a) dust emission hotspot extent and dust day occurrences (Landsat 8–9, MODIS, and MSG-SEVIRI); (b) flooding events and precipitation totals (MODIS and GPM-IMERG); and climatological parameters including (c) surface air temperature, (d) relative humidity, and (e) wind speed (ERA5-Land climate reanalysis) over Etosha Pan for 2017–2022. Grey shaded areas indicate the duration of dust emission hotspot activity and vertical grey lines mark individual dust emission days, displayed consistently across all panels. The horizontal line in panel (e) indicates the approximate 10 m wind speed threshold (~6 m s^{-1}) associated with dust emission from Etosha Pan.

formation and destabilization of these surface crusts is therefore critical to understanding the spatiotemporal development of emission hotspot regions within broader playa dust sources.

The interannual variability in dust emission hotspots across Etosha Pan is illustrated in Figure 7 alongside regional hydrometeorological conditions. Emissive activity was recorded during the dry seasons of 2018, 2019, and 2022, whereas the dry seasons of 2020 and 2021 were notably non-emissive. While the spatial extent and distribution of hotspots varied across emissive years, their timing and duration were consistently regulated by seasonal precipitation and surface moisture dynamics (Figures 7a and 7b). Hotspots typically emerged between May and June, following the onset of the austral winter dry season, and persisted until the onset of the austral summer wet season began between October and November.

As shown in Figure 7b, mean daily precipitation across the central pan during wet seasons of emissive years (2018, 2019, 2022; average 1.83 mm ± 4.13 mm) was lower than during non-emissive years 2020 (3.24 mm ± 7.43 mm) and 2021 (2.96 mm ± 7.04 mm). Pan flooding was also more frequent and extensive in 2020 (eight events) and 2021 (four events) than in emissive years (one to two events; Figure 7b). In emissive years, hotspot development consistently followed a drying phase of 1–3 months after precipitation and

2–5 months after flooding events (Figures 7a and 7b). In non-emissive years, prolonged wet conditions into the dry season maintained residual surface water into April–May, limiting dust emissions (three dust days in 2020; six in 2021; Figure 7a) and preventing the development of visually or mineralogically distinct hotspots.

Despite variations in precipitation and flooding regimes, widespread halite-rich crusts were detected in all dry seasons between 2018 and 2022 (Figures 5 and 6; Figures S3–S5 in Supporting Information S1). This indicates that crust formation is not solely dependent on salt redistribution from flooding, as observed in other playas (e.g., Artieda et al., 2015; Bowen et al., 2017; Mees, 1999). Rather, capillary-driven evaporation from shallow groundwater (0–3 m) and nocturnal humidity cycles likely play key roles in crust formation through salt efflorescence (Buck et al., 2011; Goodall et al., 2000; Reynolds et al., 2007). Diurnal temperature variations typical of the dry season, where night-time cooling promotes brine formation through deliquescence followed by daytime warming driving salt crystallization, are particularly important for producing weak, emissive crusts (Nield, Neuman, et al., 2016; Nield, Wiggs, et al., 2016; Milewski et al., 2020).

In emissive years (2018, 2019, 2022), crust formation occurred earlier in the dry season (March–April), coinciding with cooler temperatures (~15°–25°C; Figure 7c) and higher Relative humidity (RH) (>60%; Figure 7d), conditions conducive to the development of loose, efflorescent evaporite crusts susceptible to aeolian erosion (Gillette et al., 2001; Reynolds et al., 2007, 2009). Crusts formed under these conditions were strongly associated with the development of dust emission hotspot regions during periods of increased aeolian activity. Dust emission events from these regions occurred when daily wind velocities exceeded ~6 m s^{-1} at 10 m height (Figure 7e), aligning with critical thresholds reported in previous studies (e.g., Murray et al., 2016; Vickery et al., 2013; Wallum et al., 2025, 2026) and associated with low-level jet activity (Clements & Washington, 2021; Wiggs et al., 2022).

In contrast, during non-emissive years (2020 and 2021), elevated surface and subsurface moisture from antecedent precipitation and flooding delayed desiccation and subsequent formation of evaporative crusts. The late dry season formation of mixed halite-calcite crusts (August–September) under warmer (~30°C; Figure 7c), drier (~10%–20% RH; Figure 7d) conditions may have reduced the susceptibility to wind erosion. Microstructural characteristics, particularly salt crystal habit, are strongly influenced by the environmental conditions during crust formation, including soil moisture, temperature, and humidity (Dai et al., 2022; Warren, 2010, 2016). Without the nocturnal moisture input typical of cooler, more humid periods of earlier dry seasons, these mixed halite-calcite crusts may have developed into denser, interlocking surfaces with greater cohesion (Buck et al., 2011; Goldstein et al., 2017; Langston & McKenna Neuman, 2005). Repeated rehydration and dehydration cycles can further modify salt morphology, enhancing crust integrity and resistance to deflation (Gillette et al., 2001; Lee & Kurtis, 2017; Zhang et al., 2021). Field and laboratory studies confirm that halite-dominated playa crusts formed under prolonged aridity and low humidity can develop into continuous, erosion-resistant surfaces that inhibit dust emission (Gill, 1996; McLaurin et al., 2011; Pelletier & Cook, 2005; Quick & Chadwick, 2011; Reynolds et al., 2007). It is plausible that these processes occurred at Etosha Pan in 2020 and 2021, preventing dust source activation despite the occurrence of erosive winds. Although seasonal elevations in daily wind speeds in 2020 and 2021 were comparable to emissive years (6–8 m s^{-1}), dust emissions were infrequent and did not result in persistent hotspot formation (Figure 7e).

In addition to these seasonal-scale differences, interannual variability in diurnal conditions (Figures 7c and 7d) may contribute to variations in surface erodibility. Across 2018–2022, both the day–night temperature difference (ΔT) and the day–night RH difference (ΔRH) were consistently smaller in emissive years. Average ΔT ranged from 3.08°C (2022) to 3.26°C (2019) in emissive years, compared to 3.36°C (2020) and 3.49°C (2021) in non-emissive years. Average ΔRH followed the same pattern, with emissive years ranging from 5.85% (2019) to 6.37% (2018) versus 8.44% (2020) and 9.27% (2021) in non-emissive years. These reductions (on the order of 0.1°–0.4°C for ΔT and 2.0%–3.0% for ΔRH) may reflect more stable overnight atmospheric conditions during dusty years. This pattern aligns with the crust stability framework of Milewski et al. (2020), where reduced nocturnal cooling and weaker humidity recovery limit overnight crust rehydration and strengthening. Under such conditions, efflorescent mixed halite crusts remain friable for longer, maintaining a readily entrainable dust supply. Conversely, larger diurnal swings in non-emissive years likely reflect stronger radiative cooling and higher nighttime humidity, promoting thin wetting films or recrystallization that temporarily armor the surface. These diurnal effects may shorten the interval between post-flood crust formation and destabilization in emissive years, extending the seasonal window for dust release, and could be further enhanced by dust–radiation feedbacks that reduce diurnal variability (Milewski et al., 2020). The absolute temperature and RH conditions may also be important, as transitions between evaporite mineral stability thresholds can promote repeated crystallization and dissolution cycles that weaken surface crusts (Nield, Wiggs, et al., 2016). Although the temperature and humidity records shown in Figure 7 are broadly consistent with conditions that may influence such transitions, direct assessment of mineral-specific stability thresholds and phase changes was beyond the scope of the present study.

Taken together, the results highlight a series of interacting climatic controls on dust emission from Etosha Pan. At the broadest scale, antecedent precipitation and flooding (Figure 7b) determine whether and when crusts can form. Seasonal temperature and humidity conditions during crust formation (Figures 7c and 7d) influence the type of crust produced, ranging from friable efflorescent crusts formed under cool, humid early dry-season conditions to dense, cohesive surfaces formed under hot, dry late dry-season conditions. Superimposed on these broader controls are diurnal-scale effects (Figures 7c and 7d), where reduced differences between day and night temperature and humidity limit overnight crust rehydration and strengthening. These conditions accelerate surface weakening and prolong emissivity by maintaining friable crusts more prone to wind entrainment. The interplay between hydrological setting, seasonal climate, and diurnal atmospheric stability thus governs pan surface erodibility and dust emission potential.

While this study provides robust evidence for the climatic regulation of dust emissivity based on satellite remote sensing and reanalysis data, a comprehensive understanding of the mineralogical and microstructural properties of the pan surface remains limited. In situ monitoring is essential to resolve the complex interactions among hydrological processes (such as precipitation and flooding), local meteorological conditions (including temperature and humidity), and their combined influence on efflorescent salt crust formation and subsurface properties (such as crust thickness, soil structure, and mineral composition). Such knowledge is critical for determining the specific conditions that govern surface susceptibility to wind erosion. Nonetheless, these findings underscore the importance of crust formation timing, modulated by seasonal and diurnal hydrometeorological conditions, as a key determinant of dust source activation from this globally significant ephemeral lake bed.

5. Conclusions

This study advances understanding of dust emission dynamics in ephemeral saline playa systems by identifying the mineralogical and hydroclimatic controls on source activation at Etosha Pan, Namibia. Using an integrated approach that combines satellite remote sensing, reanalysis data, field observations, and laboratory analyses of surface sediments, we show that dust emissions are spatially heterogeneous and originate from discrete, temporally variable hotspots formed through deflation of efflorescent salt crusts under specific environmental conditions. Point pattern analysis revealed clustered hotspots (1–30 km in diameter) during dry seasons of emissive years (2018, 2019, 2022) that were absent in non-emissive years (2020, 2021). Mineralogical analyses (XRD and spectral unmixing) indicate that these hotspots are characterized by exposed subsurface clay- and silicate-rich sediments (e.g., analcime, montmorillonite, muscovite, saponite) beneath evaporite crusts dominated by halite and calcite. These results provide the first direct mineralogical characterization of dust sources at Etosha Pan and demonstrate the utility of remote mineral mapping for identifying emission-prone surfaces. We also show that hydrological variability governs crust evolution and dust emission dynamics. Seasonal flooding and desiccation drive crust formation and breakdown, with early dry-season desiccation facilitating deflation during peak wind periods in emissive years. In contrast, delayed desiccation and crust development in non-emissive years suppressed emissions despite favorable wind conditions. Crust erodibility is further modulated by surface moisture, air temperature, and RH at the time of formation, all of which influence crust cohesion and structural integrity. Collectively, these findings provide a process-based framework for understanding dust source dynamics in saline playa environments and underscore the importance of incorporating salt crust processes and hydroclimatic controls into dust emission models to improve projections of dust flux and related impacts under future climate scenarios. The integrated methodology presented here is readily transferable to other dust-bearing ephemeral lake systems where surface mineralogy and crust dynamics exert a strong influence on dust emission processes.

Inclusion in Global Research Statement

This research was conducted in collaboration with Namibian institutions and personnel, including the Etosha Ecological Institute and Etosha National Park, under National Commission on Research, Science and Technology

(NCRST) Permit No. RPIV00122018. Local expertise, logistical support, and access permissions were integral to the successful completion of the field component of this study.

Conflict of Interest

The authors declare no conflicts of interest relevant to this study.

Availability Statement

The data used in this study are available from the Oxford University Research Archive. Dust plume events and hydrological variables (precipitation and lake inundation extents) for 2000–2022 are available from Wallum (2025a), and dust emission hotspot extents and climate variables (temperature, relative humidity, and wind speed) for 2017–2022 are available from Wallum (2025b). The underlying satellite and reanalysis products used to generate these data sets are publicly available from their respective archives: MODIS Collection 6.1 Surface Reflectance products (MOD09GA and MYD09GA; Vermote & Wolfe, 2021a, 2021b) are available from NASA's Level-1 and Atmosphere Archive and Distribution System Distributed Active Archive Center (LAADS DAAC; https://ladsweb.modaps.eosdis.nasa.gov/); Landsat 8–9 Collection 2 Level-2 Surface Reflectance products (U.S. Geological Survey, 2020) are available from the U.S. Geological Survey EarthExplorer archive (https://earthexplorer.usgs.gov/); Integrated Multi-satellite Retrievals for GPM (GPM-IMERG) daily precipitation products (Huffman et al., 2019) are available from NASA's Goddard Earth Sciences Data and Information Services Center (GES DISC; https://disc.gsfc.nasa.gov/); and ERA5-Land reanalysis data (Muñoz Sabater, 2019) are available from the Copernicus Climate Change Service Climate Data Store (CDS; https://cds.climate.copernicus.eu/). Mineralogical XRD data are available from the U.S. Geological Survey ScienceBase repository (Leidelmeijer, 2026).

Acknowledgments
The authors thank Dr George Breit and Ms Heather Lowers of the U.S. Geological Survey (USGS) for providing additional insights and expertise through scanning electron microscopy with energy-dispersive X-ray spectroscopy (SEM-EDX) analyses of field sediment samples. Funding for this research was provided by the Natural Environment Research Council Doctoral Training Partnership (NERC DTP), part of UK Research and Innovation (UKRI), under Grant NE/S007474/1/228493; Hertford College, University of Oxford; the John Fell Fund, University of Oxford (Grant 0005174); and the Royal Geographical Society (with the Institute of British Geographers) Small Research Grant (SRG 15/17). Fieldwork was conducted under National Commission on Research, Science and Technology (NCRST) Permit No. RPIV00122018. The authors gratefully acknowledge the support of The Honourable Pohamba Shifeta (Minister of Environment and Tourism), Mr Pierre du Preez (Deputy Director, Etosha National Park), Mr Kenneth Uiseb (Deputy Director, Wildlife Research and Monitoring), Ms Claudine Cloete (Chief Conservation Scientist, Etosha Ecological Institute), and all staff of the Etosha Ecological Institute and Etosha National Park for their permissions and logistical support during field campaigns. The authors also thank Jan du Preez of Namibia Helicopter Services for aerial field support. Any use of trade, firm, or product names is for descriptive purposes only and does not imply endorsement by the U.S. Government.

References

Aboagye-Okyere, A., Meidan, D., Hamilton, D. S., Hess, P., Kalashnikova, O., Garay, M., & Mahowald, N. M. (2025). The changing role of dust and open fires PM2. 5 on Africa's air quality and human health. *Environmental Research Letters*, *20*(9), 094013. https://doi.org/10.1088/1748-9326/adf07e

Adebiyi, A. A., Kok, J. F., Murray, B. J., Ryder, C. L., Stuut, J. B. W., Kahn, R. A., et al. (2023). A review of coarse mineral dust in the Earth system. *Aeolian Research*, *60*, 100849. https://doi.org/10.1016/j.aeolia.2022.100849

Alduchov, O. A., & Eskridge, R. E. (1996). Improved Magnus form approximation of saturation vapor pressure. *Journal of Applied Meteorology, 1988–2005*(4), 601–609. https://doi.org/10.1175/1520-0450(1996)035<0601:IMFAOS>2.0.CO;2

Artieda, O., Davila, A., Wierzchos, J., Buhler, P., Rodríguez-Ochoa, R., Pueyo, J., & Ascaso, C. (2015). Surface evolution of salt-encrusted playas under extreme and continued dryness. *Earth Surface Processes and Landforms*, *40*(14), 1939–1950. https://doi.org/10.1002/esp.3771

Baddock, M. C., Bryant, R. G., Acosta, M. D., & Gill, T. E. (2021). Understanding dust sources through remote sensing: Making a case for CubeSats. *Journal of Arid Environments*, *184*, 104335. https://doi.org/10.1016/j.jaridenv.2020.104335

Baddock, M. C., Bullard, J. E., & Bryant, R. G. (2009). Dust source identification using MODIS: A comparison of techniques applied to the Lake Eyre Basin, Australia. *Remote Sensing of Environment*, *113*(7), 1511–1528. https://doi.org/10.1016/j.rse.2009.03.002

Baddock, M. C., Parsons, K., Strong, C., Leys, J., & McTainsh, G. (2015). Drivers of Australian dust: A case study of frontal winds and dust dynamics in the lower Lake Eyre basin. *Earth Surface Processes and Landforms*, *40*(14), 1982–1988. https://doi.org/10.1002/esp.3773

Baddock, M. C., Zobeck, T. M., Van Pelt, R. S., & Fredrickson, E. L. (2011). Dust emissions from undisturbed and disturbed, crusted playa surfaces: Cattle trampling effects. *Aeolian Research*, *3*(1), 31–41. https://doi.org/10.1016/j.aeolia.2011.03.007

Banks, J. R., Heinold, B., & Schepanski, K. (2022). Impacts of the desiccation of the Aral Sea on the Central Asian dust life-cycle. *Journal of Geophysical Research: Atmospheres*, *127*(21), e2022JD036618. https://doi.org/10.1029/2022JD036618

Bhattachan, A., D'Odorico, P., & Okin, G. S. (2015). Biogeochemistry of dust sources in Southern Africa. *Journal of Arid Environments*, *117*, 18–27. https://doi.org/10.1016/j.jaridenv.2015.02.013

Bowen, B. B., Kipnis, E. L., & Raming, L. W. (2017). Temporal dynamics of flooding, evaporation, and desiccation cycles and observations of salt crust area change at the Bonneville Salt Flats, Utah. *Geomorphology*, *299*, 1–11. https://doi.org/10.1016/j.geomorph.2017.09.036

Breit, G. N. (2022). Email to Natasha Wallum and Richard Reynolds, 12 September.

Bryant, R. G. (1996). Validated linear mixture modelling of Landsat TM data for mapping evaporite minerals on a playa surface: Methods and applications. *International Journal of Remote Sensing*, *17*(2), 315–330. https://doi.org/10.1080/01431169608949008

Bryant, R. G. (2003). Monitoring hydrological controls on dust emissions: Preliminary observations from Etosha Pan, Namibia. *Geographical Journal*, *169*(2), 131–141. https://doi.org/10.1111/1475-4959.04977

Buch, M. W., & Rose, D. (1996). Mineralogy and geochemistry of the sediments of the Etosha Pan Region in northern Namibia: A reconstruction of the depositional environment. *Journal of African Earth Sciences*, *22*(3), 355–378. https://doi.org/10.1016/0899-5362(96)00020-6

Bucher, E. H., & Stein, A. F. (2016). Large salt dust storms follow a 30-year rainfall cycle in the Mar Chiquita Lake (Córdoba, Argentina). *PLoS One*, *11*(6), e0156672. https://doi.org/10.1371/journal.pone.0156672

Buck, B. J., King, J., & Etyemezian, V. (2011). Effects of salt mineralogy on dust emissions, Salton Sea, California. *Soil Science Society of America Journal*, *75*(5), 1971–1985. https://doi.org/10.2136/sssaj2011.0049

Buck, B. J., Wolff, K., Merkler, D. J., & McMillan, N. J. (2006). Salt mineralogy of Las Vegas Wash, Nevada: Morphology and subsurface evaporation. *Soil Science Society of America Journal*, *70*(5), 1639–1651. https://doi.org/10.2136/sssaj2005.0276

Bullard, J., Baddock, M. C., McTainsh, G., & Leys, J. (2008). Sub-basin scale dust source geomorphology detected using MODIS. *Geophysical Research Letters*, *35*(15). https://doi.org/10.1029/2008GL033928

Chappell, A., Webb, N. P., Hennen, M., Zender, C. S., Ciais, P., Schepanski, K., et al. (2023). Elucidating hidden and enduring weaknesses in dust emission modeling. *Journal of Geophysical Research: Atmospheres*, *128*(17), e2023JD038584. https://doi.org/10.1029/2023JD038584

Clements, M., & Washington, R. (2021). Atmospheric controls on mineral dust emission from the Etosha Pan, Namibia: Observations from the CLARIFY-2016 field campaign. *Journal of Geophysical Research: Atmospheres*, *126*(14), e2021JD034746. https://doi.org/10.1029/2021JD034746

Cogliati, S., Sarti, F., Chiarantini, L., Cosi, M., Lorusso, R., Lopinto, E., et al. (2021). The PRISMA imaging spectroscopy mission: Overview and first performance analysis. *Remote Sensing of Environment*, *262*, 112499. https://doi.org/10.1016/j.rse.2021.112499

Crowley, J. K. (1991). Visible and near-infrared (0.4–2.5 μm) reflectance spectra of playa evaporite minerals. *Journal of Geophysical Research*, *96*(B10), 16231–16240. https://doi.org/10.1029/91JB01714

Cunningham, P. L., & Jankowitz, W. (2010). A review of fauna and flora associated with coastal and inland saline flats from Namibia with special reference to the Etosha Pan. In M. Öztürk, B. Böer, H. J. Barth, M. Clüsener-Godt, M. Khan, & S. W. Breckle (Eds.), *Sabkha ecosystems. Tasks for vegetation science* (Vol. 46, pp. 9–17). Springer. https://doi.org/10.1007/978-90-481-9673-9_2

Dai, J., Zhang, G., Liu, L., Shi, P., Zhang, H., Han, X., et al. (2022). Effects of efflorescence and subflorescence by different salts on soil physical properties and aeolian erosion. *Catena*, *215*, 106323. https://doi.org/10.1016/j.catena.2022.106323

Dansie, A. P., Thomas, D. S., Wiggs, G. F. S., Baddock, M. C., & Ashpole, I. (2022). Plumes and blooms–Locally-sourced Fe-rich Aeolian mineral dust drives phytoplankton growth off southwest Africa. *Science of the Total Environment*, *829*, 154562. https://doi.org/10.1016/j.scitotenv.2022.154562

De Deckker, P. (2019). An evaluation of Australia as a major source of dust. *Earth-Science Reviews*, *194*, 536–567. https://doi.org/10.1016/j.earscirev.2019.01.008

Drake, N. A., Bryant, R. G., Millington, A. C., & Townshend, J. R. (1994). Playa sedimentology and geomorphology: Mixture modelling applied to Landsat thematic mapper data of Chott el Djerid, Tunisia. *Sedimentology and Geochemistry of Modern and Ancient Saline Lakes*, 125–131. https://doi.org/10.2110/pec.94.50.0125

Ferrier, G., White, K., Griffiths, G., Bryant, R. G., & Stefouli, M. (2002). The mapping of hydrothermal alteration zones on the island of Lesvos, Greece using an integrated remote sensing dataset. *International Journal of Remote Sensing*, *23*(2), 341–356. https://doi.org/10.1080/01431160010003857

Formenti, P., D'Anna, B., Flamant, C., Mallet, M., Piketh, S. J., Schepanski, K., et al. (2019). The aerosols, radiation and clouds in southern Africa field campaign in Namibia: Overview, illustrative observations, and way forward. *Bulletin of the American Meteorological Society*, *100*(7), 1277–1298. https://doi.org/10.1175/BAMS-D-17-0278.1

Geological Survey, U. S. (2020). Landsat 8-9 collection 2 Level-2 science products [Dataset]. *U.S. Geological Survey*. https://www.usgs.gov/landsat-missions

Gill, T. E. (1996). Eolian sediments generated by anthropogenic disturbance of playas: Human impacts on the geomorphic system and geomorphic impacts on the human system. *Geomorphology*, *17*(1–3), 207–228. https://doi.org/10.1016/0169-555X(95)00104-D

Gillette, D. A. (1999). A qualitative geophysical explanation for "hot spot" dust emitting source regions. *Contributions to Atmospheric Physics*, *72*(1), 67–77.

Gillette, D. A., Niemeyer, T. C., & Helm, P. J. (2001). Supply-limited horizontal sand drift at an ephemerally crusted, unvegetated saline playa. *Journal of Geophysical Research*, *106*(D16), 18085–18098. https://doi.org/10.1029/2000JD900324

Goldstein, H. L., Breit, G. N., & Reynolds, R. L. (2017). Controls on the chemical composition of saline surface crusts and emitted dust from a wet playa in the Mojave Desert (USA). *Journal of Arid Environments*, *140*, 50–66. https://doi.org/10.1016/j.jaridenv.2017.01.010

González-Romero, A., González-Flórez, C., Panta, A., Yus-Díez, J., Córdoba, P., Alastuey, A., et al. (2024). Characterization of the particle size distribution, mineralogy, and Fe mode of occurrence of dust-emitting sediments from the Mojave Desert, California, USA. *Atmospheric Chemistry and Physics*, *24*(16), 9155–9176. https://doi.org/10.5194/acp-24-9155-2024

Goodall, T. M., North, C. P., & Glennie, K. W. (2000). Surface and subsurface sedimentary structures produced by salt crusts. *Sedimentology*, *47*(1), 99–118. https://doi.org/10.1046/j.1365-3091.2000.00279.x

Goudie, A. S. (2018). Dust storms and ephemeral lakes. *Desert*, *23*(1), 153–164.

Green, R. O., Mahowald, N. M., Thompson, D. R., Clark, R., Ehlmann, B., Ginoux, P., et al. (2019). The Earth surface mineral dust source investigation planned for the international space station. *Geophysical Research Abstracts*, *21*, 1.

Green, R. O., Mahowald, N. M., Thompson, D. R., Ung, C., Brodrick, P., Pollock, R., et al. (2023). Performance and early results from the Earth surface mineral dust source investigation (EMIT) imaging spectroscopy mission. *2023 IEEE Aerospace Conference*, 1–10.

Hamilton, D. S., Perron, M. M., Bond, T. C., Bowie, A. R., Buchholz, R. R., Guieu, C., et al. (2022). Earth, wind, fire, and pollution: Aerosol nutrient sources and impacts on ocean biogeochemistry. *Annual Review of Marine Science*, *14*(1), 303–330. https://doi.org/10.1146/annurev-marine-031921-013612

Hamunyela, E., Hipondoka, M. H. T., Persendt, F., Nghiyalwa, H. S., Thomas, C., & Matengu, K. (2022). Spatio-temporal characterization of surface water dynamics with Landsat in endorheic Cuvelai-Etosha Basin (1990–2021). *ISPRS Journal of Photogrammetry and Remote Sensing*, *191*, 68–84. https://doi.org/10.1016/j.isprsjprs.2022.07.007

Hennen, M., Chappell, A., Webb, N. P., Schepanski, K., Baddock, M. C., Eckardt, F. D., et al. (2024). A new framework for evaluating dust emission model development using dichotomous satellite observations of dust emission. *Science of the Total Environment*, *912*, 169237. https://doi.org/10.1016/j.scitotenv.2023.169237

Hipondoka, M. H. T., Mauz, B., Kempf, J., Packman, S., Chiverrell, R. C., & Bloemendal, J. (2014). Chronology of sand ridges and the late Quaternary evolution of the Etosha Pan, Namibia. *Geomorphology*, *204*, 553–563. https://doi.org/10.1016/j.geomorph.2013.08.034

Hipondoka, M. H. T., van der Waal, B. C. W., Ndeutapo, M. H., & Hango, L. (2018). Sources of fish in the ephemeral western iishana region of the Cuvelai–Etosha Basin in Angola and Namibia. *African Journal of Aquatic Science*, *43*(3), 199–214. https://doi.org/10.2989/16085914.2018.1506310

Hubbard, B. E., & Crowley, J. K. (2005). Mineral mapping on the Chilean–Bolivian Altiplano using co-orbital ALI, ASTER and hyperion imagery: Data dimensionality issues and solutions. *Remote Sensing of Environment*, *99*(1–2), 173–186. https://doi.org/10.1016/j.rse.2005.04.027

Huffman, G. J., Stocker, E. F., Bolvin, D. T., Nelkin, E. J., & Tan, J. (2019). GPM IMERG final precipitation L3 daily 0.1° × 0.1°, version 06 [Dataset]. *NASA Goddard Earth Sciences Data and Information Services Center (GES DISC)*. https://doi.org/10.5067/GPM/IMERGDF/DAY/06

Jin, Q., Ma, Y., Pan, E., Fan, F., Huang, J., Li, H., et al. (2019). Hyperspectral unmixing with Gaussian mixture model and spatial group sparsity. *Remote Sensing*, *11*(20), 2434. https://doi.org/10.3390/rs11202434

Kandakji, T., Gill, T. E., & Lee, J. A. (2020). Identifying and characterizing dust point sources in the southwestern United States using remote sensing and GIS. *Geomorphology*, *353*, 107019. https://doi.org/10.1016/j.geomorph.2019.107019

Karami, S., Hamzeh, N. H., Kaskaoutis, D. G., Rashki, A., Alam, K., & Ranjbar, A. (2021). Numerical simulations of dust storms originated from dried lakes in central and southwest Asia: The case of Aral Sea and Sistan Basin. *Aeolian Research*, *50*, 100679. https://doi.org/10.1016/j.aeolia.2021.100679

King, J., Etyemezian, V., Sweeney, M., Buck, B. J., & Nikolich, G. (2011). Dust emission variability at the Salton Sea, California, USA. *Aeolian Research*, *3*(1), 67–79. https://doi.org/10.1016/j.aeolia.2011.03.005

Klose, M., Gill, T. E., Etyemezian, V., Nikolich, G., Zadeh, Z. G., Webb, N. P., & Van Pelt, R. S. (2019). Dust emission from crusted surfaces: Insights from field measurements and modelling. *Aeolian Research*, *40*, 1–14. https://doi.org/10.1016/j.aeolia.2019.05.001

Klose, M., Jorba, O., Gonçalves Ageitos, M., Escribano, J., Dawson, M. L., Obiso, V., et al. (2021). Mineral dust cycle in the Multiscale online nonhydrostatic AtmospheRe CHemistry model (MONARCH) version 2.0. *Geoscientific Model Development*, *14*(10), 6403–6444. https://doi.org/10.5194/gmd-14-6403-2021

Kodikara, G. R., McHenry, L. J., & van der Meer, F. D. (2023). Spectral mapping of zeolite bearing paleolake deposits at Lake Tecopa, California and its implications for mapping zeolites on Mars. *Geosystems and Geoenvironment*, *2*(1), 100119. https://doi.org/10.1016/j.geogeo.2022.100119

Kodikara, G. R., Woldai, T., van Ruitenbeek, F. J., Kuria, Z., van der Meer, F., Shepherd, K. D., & Van Hummel, G. J. (2012). Hyperspectral remote sensing of evaporate minerals and associated sediments in Lake Magadi area, Kenya. *International Journal of Applied Earth Observation and Geoinformation*, *14*(1), 22–32. https://doi.org/10.1016/j.jag.2011.08.009

Kok, J. F., Adebiyi, A. A., Albani, S., Balkanski, Y., Checa-Garcia, R., Chin, M., et al. (2021a). Improved representation of the global dust cycle using observational constraints on dust properties and abundance. *Atmospheric Chemistry and Physics*, *21*(10), 8127–8167. https://doi.org/10.5194/acp-21-8127-2021

Kok, J. F., Adebiyi, A. A., Albani, S., Balkanski, Y., Checa-Garcia, R., Chin, M., et al. (2021b). Contribution of the world's main dust source regions to the global cycle of desert dust. *Atmospheric Chemistry and Physics*, *21*(10), 8169–8193. https://doi.org/10.5194/acp-21-8169-2021

Kok, J. F., Gupta, A., Evan, A. T., Adebiyi, A. A., Albani, S., Balkanski, Y., et al. (2025). Desert dust exerts a substantial longwave radiative forcing missing from climate models. https://doi.org/10.31223/X53B2J

Kok, J. F., Storelvmo, T., Karydis, V. A., Adebiyi, A. A., Mahowald, N. M., Evan, A. T., et al. (2023). Mineral dust aerosol impacts on global climate and climate change. *Nature Reviews Earth and Environment*, *4*(2), 71–86. https://doi.org/10.5194/acp-21-8169-2021

Kokaly, R. F., Clark, R. N., Swayze, G. A., Livo, K. E., Hoefen, T. M., Pearson, N. C., et al. (2017). USGS Spectral Library Version 7: USGS Geological survey data series 1035 [Dataset]. *United States Geological Survey*. https://doi.org/10.3133/ds1035

Kruse, F. A., & Perry, S. L. (2013). Mineral mapping using simulated Worldview-3 short-wave-infrared imagery. *Remote Sensing*, *5*(6), 2688–2703. https://doi.org/10.3390/rs5062688

Langston, G., & McKenna Neuman, C. (2005). An experimental study on the susceptibility of crusted surfaces to wind erosion: A comparison of the strength properties of biotic and salt crusts. *Geomorphology*, *72*(1–4), 40–53. https://doi.org/10.1016/j.geomorph.2005.05.003

Lawrence, M. G. (2005). The relationship between relative humidity and the dewpoint temperature in moist air: A simple conversion and applications. *Bulletin of the American Meteorological Society*, *86*(2), 225–234. https://doi.org/10.1175/BAMS-86-2-225

Lee, B. Y., & Kurtis, K. E. (2017). Effect of pore structure on salt crystallization damage of cement-based materials: Consideration of w/b and nanoparticle use. *Cement and Concrete Research*, *98*, 61–70. https://doi.org/10.1016/j.cemconres.2017.04.002

Leidelmeijer, J. A. (2026). Particle size and X-ray diffraction data for surficial samples collected on Etosha Pan [Dataset]. *Namibia: U.S. Geological Survey Data Release*. https://doi.org/10.5066/P1HLMW47

Li, L., Mahowald, N. M., Miller, R., García-Pando, C. P., Ageitos, M. G., Ginoux, P., et al. (2025). Spaceborne mineral mapping reduces dust's shortwave radiative impact uncertainty [Preprint]. https://doi.org/10.31223/X57Q97

Li, R., Liu, C., Xu, H., Jiao, P., Hu, Y., Fan, L., & Sun, X. (2020). Genesis of Glauberite sedimentation in Lop Nur salt lake–Constraints from thermodynamic simulation of the shallow groundwater in the Tarim River Basin, China. *Chemical Geology*, *537*, 119461. https://doi.org/10.1016/j.chemgeo.2019.119461

Li, Z., Wang, G., Wang, X., Wan, L., Shi, Z., Wanke, H., et al. (2018). Groundwater quality and associated hydrogeochemical processes in Northwest Namibia. *Journal of Geochemical Exploration*, *186*, 202–214. https://doi.org/10.1016/j.gexplo.2017.12.015

Macpherson, T., Nickling, W. G., Gillies, J. A., & Etyemezian, V. (2008). Dust emissions from undisturbed and disturbed supply-limited desert surfaces. *Journal of Geophysical Research*, *113*(F2). https://doi.org/10.1029/2007JF000800

Mahowald, N. M., Bryant, R. G., del Corral, J., & Steinberger, L. (2003). Ephemeral lakes and desert dust sources. *Geophysical Research Letters*, *30*(2). https://doi.org/10.1029/2002GL016041

Mateus, P., Mendes, V. B., & Plecha, S. M. (2021). HGPT2: An ERA5-based global model to estimate relative humidity. *Remote Sensing*, *13*(11), 2179. https://doi.org/10.3390/rs13112179

McLaurin, B. T., Goossens, D., & Buck, B. J. (2011). Combining surface mapping and process data to assess, predict, and manage dust emissions from natural and disturbed land surfaces. *Geosphere*, *7*(1), 260–275. https://doi.org/10.1130/GES00593.1

Mees, F. (1999). Distribution patterns of gypsum and kalistrontite in a dry lake basin of the southwestern Kalahari (Omongwa pan, Namibia). *Earth Surface Processes and Landforms: The Journal of the British Geomorphological Research Group*, *24*(8), 731–744. https://doi.org/10.1002/(SICI)1096-9837(199908)24:8<731::AID-ESP7>3.0.CO;2-0

Mees, F., & Singer, A. (2006). Surface crusts on soils/sediments of the southern Aral Sea basin, Uzbekistan. *Geoderma*, *136*(1–2), 152–159. https://doi.org/10.1016/j.geoderma.2006.03.019

Mendelsohn, J., Jarvis, A., & Robertson, T. (Eds.) (2013). *A profile and atlas of the Cuvelai-Etosha Basin* (pp. 1–166). RAISON and Gondwana Collection.

Middleton, N. J., & Kang, U. (2017). Sand and dust storms: Impact mitigation. *Sustainability*, *9*(6), 1053. https://doi.org/10.3390/su9061053

Milewski, R., Chabrillat, S., & Behling, R. (2017). Analyses of recent sediment surface dynamic of a Namibian Kalahari salt pan based on multitemporal Landsat and hyperspectral Hyperion data. *Remote Sensing*, *9*(2), 170. https://doi.org/10.3390/rs9020170

Milewski, R., Chabrillat, S., & Bookhagen, B. (2020). Analyses of Namibian seasonal salt pan crust dynamics and climatic drivers using Landsat 8 time series and ground data. *Remote Sensing*, *12*(3), 474. https://doi.org/10.3390/rs12030474

Milewski, R., Chabrillat, S., Brell, M., Schleicher, A. M., & Guanter, L. (2019). Assessment of the 1.75 µm absorption feature for gypsum estimation using laboratory, air-and spaceborne hyperspectral sensors. *International Journal of Applied Earth Observation and Geoinformation*, *77*, 69–83. https://doi.org/10.1016/j.jag.2018.12.012

Miller, R. M. G. (1997). The Owambo Basin of Northern Namibia. *Sedimentary Basins of the World*, *3*, 237–268. https://doi.org/10.1016/S1874-5997(97)80014-7

Miller, R. M. G., Pickford, M., & Senut, B. (2010). The geology, palaeontology and evolution of the Etosha Pan, Namibia: Implications for terminal Kalahari deposition. *South African Journal of Geology*, *113*(3), 307–334. https://doi.org/10.2113/gssajg.113.3.307

Mona, L., Amiridis, V., Cuevas, E., Gkikas, A., Trippetta, S., Vandenbussche, S., et al. (2023). Observing mineral dust in Northern Africa, the Middle East, and Europe: Current capabilities and challenges ahead for the development of dust services. *Bulletin of the American Meteorological Society*, *104*(12), E2223–E2264. https://doi.org/10.1175/BAMS-D-23-0005.1

Muñoz Sabater, J. (2019). ERA5-Land hourly data from 1981 to present [Dataset]. *Copernicus Climate Change Service Climate Data Store*. https://doi.org/10.24381/cds.e2161bac

Muñoz-Sabater, J., Dutra, E., Agustí-Panareda, A., Albergel, C., Arduini, G., Balsamo, G., et al. (2021). ERA5-Land: A state-of-the-art global reanalysis dataset for land applications. *Earth System Science Data*, *13*(9), 4349–4383. https://doi.org/10.5194/essd-13-4349-2021

Murray, J. E., Brindley, H. E., Bryant, R. G., Russell, J. E., Jenkins, K. F., & Washington, R. (2016). Enhancing weak transient signals in SEVIRI false color imagery: Application to dust source detection in southern Africa. *Journal of Geophysical Research: Atmospheres*, *121*(17), 10199–10219. https://doi.org/10.1002/2016JD025221

Nickling, W. G., & Ecclestone, M. (1981). The effects of soluble salts on the threshold shear velocity of fine sand. *Sedimentology*, *28*(4), 505–510. https://doi.org/10.1111/j.1365-3091.1981.tb01698.x

Nield, J. M., Bryant, R. G., Wiggs, G. F. S., King, J., Thomas, D. S., Eckardt, F. D., & Washington, R. (2015). The dynamism of salt crust patterns on playas. *Geology*, *43*(1), 31–34. https://doi.org/10.1130/G31272.1

Nield, J. M., Neuman, C. M., O'Brien, P., Bryant, R. G., & Wiggs, G. F. S. (2016). Evaporative sodium salt crust development and its wind tunnel derived transport dynamics under variable climatic conditions. *Aeolian Research*, *23*, 51–62. https://doi.org/10.1016/j.aeolia.2016.09.003

Nield, J. M., Wiggs, G. F. S., King, J., Bryant, R. G., Eckardt, F. D., Thomas, D. S., & Washington, R. (2016). Climate–surface–pore-water interactions on a salt crusted playa: Implications for crust pattern and surface roughness development measured using terrestrial laser scanning. *Earth Surface Processes and Landforms*, *41*(6), 738–753. https://doi.org/10.1002/esp.3860

Niemeyer, T. C., Gillette, D. A., DeLuisi, J. J., Kim, Y. J., Niemeyer, W. F., Ley, T., et al. (1999). Optical depth, size distribution and flux of dust from Owens Lake, California. *Earth Surface Processes and Landforms: The Journal of the British Geomorphological Research Group*, *24*(5), 463–479. https://doi.org/10.1002/(SICI)1096-9837(199905)24:5<463::AID-ESP2>3.0.CO;2-R

Pelletier, J. D., & Cook, J. P. (2005). Deposition of playa windblown dust over geologic time scales. *Geology*, *33*(11), 909–912. https://doi.org/10.1130/G22013.1

Pickford, M., Senut, B., Hipondoka, M., Person, A., Segalen, L., Plet, C., et al. (2009). Mio-pliopleistocene geology and palaeobiology of Etosha Pan. *Namibia. Communications of the geological Survey of Namibia*, *14*, 95–139.

Prospero, J. M., Delany, A. C., Delany, A. C., & Carlson, T. N. (2021). The discovery of African dust transport to the Western Hemisphere and the Saharan air layer: A history. *Bulletin of the American Meteorological Society*, *102*(6), 1–53. https://doi.org/10.1175/BAMS-D-19-0309.1

Prospero, J. M., Ginoux, P., Torres, O., Nicholson, S. E., & Gill, T. E. (2002). Environmental characterization of global sources of atmospheric soil dust identified with the Nimbus 7 total ozone mapping spectrometer (TOMS) absorbing aerosol product. *Reviews of Geophysics*, *40*(1), 2-1–31. https://doi.org/10.1029/2000RG000095

Quick, D. J., & Chadwick, O. A. (2011). Accumulation of salt-rich dust from Owens Lake playa in nearby alluvial soils. *Aeolian Research*, *3*(1), 23–29. https://doi.org/10.1016/j.aeolia.2011.03.004

Radwin, M. H., & Bowen, B. B. (2021). Mapping mineralogy in evaporite basins through time using multispectral Landsat data: Examples from the Bonneville basin, Utah, USA. *Earth Surface Processes and Landforms*, *46*(6), 1160–1176. https://doi.org/10.1002/esp.5089

Rahm, L., & Buch, M. (1997). Groundwater flow in the southern part of the Etosha basin indicated by the chemical composition of water. *Madoqua*, *1997*(1), 129–135. https://hdl.handle.net/10520/AJA10115498_464

Reynolds, R. L., Bogle, R., Vogel, J., Goldstein, H. L., & Yount, J. (2009). Dust emission at Franklin Lake Playa, Mojave Desert (USA): Response to meteorological and hydrologic changes 2005–2008. *Natural Resources and Environmental Issues*, *15*(18), 105–115. https://digitalcommons.usu.edu/nrei/vol15/iss1/18

Reynolds, R. L., Yount, J. C., Reheis, M., Goldstein, H. L., Chavez Jr, P., Fulton, R., et al. (2007). Dust emission from wet and dry playas in the Mojave Desert, USA. *Earth Surface Processes and Landforms: The Journal of the British Geomorphological Research Group*, *32*(12), 1811–1827. https://doi.org/10.1002/esp.1515

Rouse, J., Haas, R., Schell, J., & Deering, D. (1973). Monitoring vegetation systems in the Great Plains with ERTS. *Third ERTS Symposium*, *1*, 309–317.

Settle, J. J., & Drake, N. A. (1993). Linear mixing and the estimation of ground cover proportions. *International Journal of Remote Sensing*, *14*(6), 1159–1177. https://doi.org/10.1080/01431169308904402

Shaw, P. A., & Bryant, R. G. (2011). Pans, playas and salt lakes. *Arid Zone Geomorphology: Process, Form and Change in Drylands*, 373–401. https://doi.org/10.1002/9780470710777.ch15

Song, Q., & Ginoux, P. (2025). The contribution of ephemeral lakes to global dust cycle and direct radiative effect. *Geophysical Research Letters*, *52*(17), e2025GL116689. https://doi.org/10.1029/2025GL116689

Sweeney, M. R., Forman, S. L., & McDonald, E. V. (2022). Contemporary and future dust sources and emission fluxes from gypsum-and quartz-dominated Eolian systems, New Mexico and Texas, USA. *Geology*, *50*(3), 356–360. https://doi.org/10.1130/G49488.1

Sweeney, M. R., McDonald, E. V., & Etyemezian, V. (2011). Quantifying dust emissions from desert landforms, eastern Mojave Desert, USA. *Geomorphology*, *135*(1–2), 21–34. https://doi.org/10.1016/j.geomorph.2011.07.022

Sweeney, M. R., Zlotnik, V. A., Joeckel, R. M., & Stout, J. E. (2016). Geomorphic and hydrologic controls of dust emissions during drought from Yellow Lake playa, West Texas, USA. *Journal of Arid Environments*, *133*, 37–46. https://doi.org/10.1016/j.jaridenv.2016.05.007

Teller, J. T., & Last, W. M. (1990). Paleohydrological indicators in playas and salt lakes, with examples from Canada, Australia, and Africa. *Palaeogeography, Palaeoclimatology, Palaeoecology*, *76*(3–4), 215–240. https://doi.org/10.1016/0031-0182(90)90114-M

Tong, D. Q., Gill, T. E., Sprigg, W. A., Van Pelt, R. S., Baklanov, A. A., Barker, B. M., et al. (2023). Health and safety effects of airborne soil dust in the Americas and beyond. *Reviews of Geophysics*, *61*(2), e2021RG000763. https://doi.org/10.1029/2021RG000763

Vermote, E., & Wolfe, R. (2021a). MODIS/terra surface reflectance daily L2G global 1 km and 500 m SIN grid V061 [Dataset]. *NASA Land Processes Distributed Active Archive Center*. https://doi.org/10.5067/MODIS/MOD09GA.061

Vermote, E., & Wolfe, R. (2021b). MODIS/aqua surface reflectance daily L2G global 1 km and 500 m SIN grid V061 [Dataset]. *NASA Land Processes Distributed Active Archive Center*. https://doi.org/10.5067/MODIS/MYD09GA.061

Vickery, K. J., Eckardt, F. D., & Bryant, R. G. (2013). A sub-basin scale dust plume source frequency inventory for southern Africa, 2005–2008. *Geophysical Research Letters*, *40*(19), 5274–5279. https://doi.org/10.1002/grl.50968

Walker, A. L., Liu, M., Miller, S. D., Richardson, K. A., & Westphal, D. L. (2009). Development of a dust source database for mesoscale forecasting in southwest Asia. *Journal of Geophysical Research*, *114*(D18). https://doi.org/10.1029/2008JD011541

Wallum, N. S. (2025a). Atmospheric mineral dust emission and climatological variables for Etosha Pan, Namibia (2000-2022) [Dataset]. *Oxford University Research Archive*. https://doi.org/10.5287/ora-korkq2z7n

Wallum, N. S. (2025b). Atmospheric dust emission hotspots and climate variables for Etosha Pan, Namibia (2017-2022) [Dataset]. *Oxford University Research Archive*. https://doi.org/10.5287/ora-8n4amejjb

Wallum, N. S., Wiggs, G. F. S., & Bryant, R. G. (2025). Coupling global climate drivers to dust emission dynamics at Etosha Pan, Namibia. *Science of the Total Environment*, *995*, 180088. https://doi.org/10.1016/j.scitotenv.2025.180088

Wallum, N. S., Wiggs, G. F. S., Huck, R. A., Leidelmeijer, J. A., & Goldstein, H. (2026). The influence of surface crust dynamics and sediment availability on Aeolian dust emission from ephemeral lake beds: Evidence from Etosha Pan, Namibia. *Aeolian Research*, *77*(10164), 101064. https://doi.org/10.1016/j.aeolia.2026.101064

Warren, J. K. (2010). Evaporites through time: Tectonic, climatic and Eustatic controls in marine and nonmarine deposits. *Earth-Science Reviews*, *98*(3–4), 217–268. https://doi.org/10.1016/j.earscirev.2009.11.004

Warren, J. K. (Ed.) (2016). *Evaporites: A geological compendium* (2nd ed.). Springer.

Washington, R., Todd, M., Middleton, N. J., & Goudie, A. S. (2003). Dust-storm source areas determined by the total ozone monitoring spectrometer and surface observations. *Annals of the Association of American Geographers*, *93*(2), 297–313. https://doi.org/10.1111/1467-8306.9302003

White, K., & Eckardt, F. D. (2006). Geochemical mapping of carbonate sediments in the Makgadikgadi basin, Botswana using moderate resolution remote sensing data. *Earth Surface Processes and Landforms*, *31*(6), 665–681. https://doi.org/10.1002/esp.1289

Wiggs, G. F. S., Baddock, M. C., Thomas, D. S. G., Washington, R., Nield, J. M., Engelstaedter, S., et al. (2022). Quantifying mechanisms of Aeolian dust emission: Field measurements at Etosha Pan, Namibia. *Journal of Geophysical Research: Earth Surface*, *127*(8), e2022JF006675. https://doi.org/10.1029/2022JF006675

Xu, H. (2006). Modification of normalised difference water index (NDWI) to enhance open water features in remotely sensed imagery. *International Journal of Remote Sensing*, *27*(14), 3025–3033. https://doi.org/10.1080/01431160600589179

Zhang, G., Xiao, Y., Xiang, M., Hong, C., Zhang, B. T., Liu, L., et al. (2021). Structure and morphological characteristics of polygonal salt crust, the West Juyan Lake, China. *Geosciences Journal*, *26*(3), 1–12. https://doi.org/10.1007/s12303-021-0037-z

Zucca, C., Middleton, N., Kang, U., & Liniger, H. (2021). Shrinking water bodies as hotspots of sand and dust storms: The role of land degradation and sustainable soil and water management. *Catena*, *207*, 105669. https://doi.org/10.1016/j.catena.2021.105669